Mechanical coupling coordinates microtubule growth

Bonnibelle K. Leeds, Katelyn F. Kostello, Yuna Y. Liu, Sue Biggins, and Charles L. Asbury

Abstract

During mitosis, kinetochore-attached microtubules form bundles (k-fibers) in which many filaments grow and shorten in near-perfect unison to align and segregate each chromosome. However, individual microtubules grow at intrinsically variable rates, which must be tightly regulated for a k-fiber to behave as a single unit. This exquisite coordination might be achieved biochemically, via selective binding of polymerases and depolymerases, or mechanically, because k-fiber microtubules are coupled through a shared load that influences their growth. Here, we use a novel dual laser trap assay to show that microtubule pairs growing *in vitro* are coordinated by mechanical coupling. Kinetic analyses show that microtubule growth is interrupted by stochastic, force-dependent pauses and indicate persistent heterogeneity in growth speed during non-pauses. A simple model incorporating both force-dependent pausing and persistent growth speed heterogeneity explains the measured coordination of microtubule pairs without any free fit parameters. Our findings illustrate how microtubule growth may be synchronized during mitosis and provide a basis for modeling k-fiber bundles with three or more microtubules, as found in many eukaryotes.

Introduction

In the mitotic spindles of many eukaryotes, each chromosome is attached to a bundle of microtubules (Kiewisz et al., 2022; McDonald et al., 1992; O'Toole et al., 2020; VandenBeldt et al., 2006) that grow and shorten in unison, acting as a single unit to produce the forces necessary to move the chromosome (Cimini et al., 2004). Microtubules are microns-long protein polymers composed of αβ-tubulin dimers with their 'minus' ends oriented toward the spindle poles and their more dynamic 'plus' ends oriented toward the chromosomes. Microtubule plus-ends, or tips, attach to chromosomes via protein complexes called kinetochores to form 'k-fiber' bundles. Kinetochore-attached tips within a single k-fiber remain very close to one another (within ~0.2 µm along the bundle axis) (O'Toole et al., 2020) even as the bundle grows and shrinks (Cimini et al., 2004) by the addition and loss of tubulin subunits at each tip (Maddox et al., 2003). Uncovering how the tips within a k-fiber maintain such a high degree of synchrony is critical to understanding how chromosomes are accurately segregated during normal mitosis and why even modest perturbations of kinetochore-attached microtubule dynamics can lead to mis-segregation (Bakhoum & Compton, 2012; Bakhoum et al., 2009; Ertych et al., 2014; Stumpff et al., 2014).

The tightly coordinated growth of microtubules within a k-fiber bundle is remarkable because individually, microtubule tips exhibit highly variable growth speeds and switch stochastically between

distinct states of growth and shortening (Brouhard, 2015). Microtubule growth speed varies considerably in purified tubulin systems (Figure 1a) (Cleary et al., 2022; Gildersleeve et al., 1992; Mahserejian et al., 2022), in cell extracts (Geisterfer et al., 2020), and in live cells (Cassimeris et al., 1988; Gaudenz et al., 2010; Yamashita et al., 2015). Part of this heterogeneity can be attributed to pausing, when microtubules stochastically stop and start growing during periods of net growth (Amoah-Darko & White, 2022; Mahserejian et al., 2022). How the intrinsic heterogeneity of microtubule growth is coordinated to maintain sub-micrometer proximity between k-fiber tips remains a mystery.

One possible mechanism that might coordinate k-fiber microtubules is selective binding of microtubule-regulatory proteins (Maiato, Rieder, et al., 2003; McAinsh & Meraldi, 2011; Tirnauer et al., 2002). Many microtubule-associated proteins that are known to regulate growth *in vitro* are implicated in modulating k-fiber dynamics and kinetochore movements in cells, including TOG-family proteins such as XMAP215 (Brouhard et al., 2008) and CLASP (Al-Bassam et al., 2010; Maiato, Fairley, et al., 2003; Sousa et al., 2007), mitotic kinesins such as MCAK and Kif18A (Sanhaji et al., 2011; Stumpff et al., 2012), and other plus-end-trackers such as EB1 (reviewed in (Amin et al., 2019)). The localization of some of these regulators is enriched near kinetochores specifically when a kinetochore is moving anti-poleward and its k-fiber is growing longer (Amaro et al., 2010; Castrogiovanni et al., 2021; Tirnauer et al., 2002). However, whether such selective enrichment is sufficient to explain the very tight coordination across many individual microtubule tips within a k-fiber is unclear.

Another, simpler mechanism is suggested by the fact that microtubule dynamics are also strongly affected by mechanical force. Tension applied to individual microtubules *in vitro* biases them toward growth (Figure 1a) (Akiyoshi et al., 2010), while compression biases them toward shortening (Dogterom & Yurke, 1997; Janson et al., 2003). Theoretically, these mechanical effects should promote synchronization of any group of microtubules whose tips, like the tips of kinetochore-attached microtubules within a k-fiber, are all coupled to the same load (Banigan et al., 2015; Schwietert & Kierfeld, 2020; Skibbens et al., 1993). To illustrate how, consider a hypothetical k-fiber composed of just two microtubules sharing a total load, F_{TOT}. The load is transmitted to the microtubule tips through the kinetochore, which has elasticity (Cojoc et al., 2016; Renda et al., 2020) that we represent as spring-like connections from the kinetochore to each tip (Figure 1b). Initially, the two microtubules might have equal lengths and share the load equally – each one carries half of F_{TOT} (Figure 1b, step 1). If one tip happens to grow more slowly than the other, then its spring will be stretched more, and it will start carrying more tension than the other tip (Figure 1b, step 2). Conversely, the faster-growing tip will start carrying less tension. Because tension accelerates microtubule growth, the lagging tip will tend to accelerate, while the leading tip will tend to slow down, such that, on average, they return to having equal lengths and tensions (Figure 1b, step 3).

Mechanical coupling was proposed decades ago as an explanation for sister k-fiber coordination (Gardner et al., 2005; Khodjakov et al., 1996; Skibbens et al., 1995; Skibbens et al., 1993; Wan et al., 2012), but how effectively it can coordinate microtubules within a k-fiber has not been determined. Compressive forces can cause a bundle of microtubules growing *in vitro* to switch cooperatively into a shortening state (Laan et al., 2008), but k-fiber bundles are usually under tension, not compression

(Khodjakov & Rieder, 1996; Waters et al., 1996). Theoretical studies have explored the effects of shared tensile and compressive loads on cooperative switching and bi-stability in microtubule bundles (Banigan et al., 2015; Das et al., 2014; Ghanti & Chowdhury, 2015; Schwietert & Kierfeld, 2020; Zelinski & Kierfeld, 2013), but these studies have generally neglected the variability in microtubule growth speed and therefore cannot address how such variability is suppressed. Furthermore, to our knowledge, the possibility that part of this variability (and suppression thereof) can be attributed to tension-dependent pausing during microtubule growth has not been explored.

Here, we use a novel dual laser trap assay to test directly how well a constant shared load can coordinate a pair of microtubules growing *in vitro*. We show that when microtubule pairs are mechanically coupled to a single load through a material of sufficient stiffness, their growth is tightly coordinated. By re-analyzing recordings of individual microtubules growing under constant force (from (Akiyoshi et al., 2010)) and examining their stochastic pausing kinetics, we show that pausing is suppressed by tension. We then develop a theoretical model, based on the measured behaviors of individual growing microtubules, to describe both the natural variability and force dependence of growth using no free fit parameters. Simulations based on this model, which incorporates stochastic, force-sensitive pausing and intrinsic variability in microtubule growth speed, fit the dual-trap data well. Altogether, this work illustrates how mechanical coupling may coordinate microtubule growth and provides a basis for modeling k-fibers of three or more microtubules under a shared load.

Results

Dual-trap assay to measure coordination between paired microtubules *in vitro*

To study how mechanical coupling affects microtubule growth, we developed a novel technique which we call the dual-trap assay (Figure 2). The dual-trap assay is based on our previously developed single-trap (force-clamp) assay (Akiyoshi et al., 2010; Miller et al., 2016; Sarangapani et al., 2013), in which dynamic microtubules are grown from stabilized seeds bound to a biotinylated coverslip. Using the single laser trap, we attach an individual bead decorated with isolated yeast kinetochores to the growing plus-end of a single microtubule. A computer then continuously measures the bead position and adjusts the trap to exert a precise, constant level of tension on the microtubule via the kinetochore-decorated bead. Under this persistent feedback-controlled tension, kinetochore-beads typically track with the microtubule tips even as the tips stochastically grow and shorten.

Our new dual-trap assay uses two separate laser trapping microscopes, located adjacent to one another in the same room and connected to a single computer. On each of the two instruments, we attach a kinetochore-decorated bead to a dynamic microtubule plus-end. The computer then simultaneously monitors and controls the forces on both microtubules. Rather than keeping the force constant on each microtubule, the computer adjusts the forces dynamically to simulate an elastic coupling of both plus-ends to a single shared load (Figure 2a). Thus far, we have simulated only purely elastic couplers, where both coupling springs are linear (Hookean) with stiffness, κ (Figure 2b). In the

future, more complex coupling materials with viscoelasticity (Cojoc et al., 2016) or strain-stiffening (Schwietert et al., 2022; Volkov et al., 2018) could also be simulated.

To begin a dual-trap experiment, we first choose the spring stiffness, κ, and the total shared load, F_{TOT}, which are kept constant (Figure 2a, step 1). After a kinetochore-decorated bead is attached to a growing plus-end on each of the two instruments, feedback-control is initiated and the two plus-ends are arbitrarily considered to be parallel, with tips side-by-side (i.e., both at $x_1 = x_2 = 0$) and sharing the load equally ($F_1 = F_2 = ½·F_{TOT}$) (Figure 2a, step 2). Because microtubule growth is intrinsically variable, the two microtubules subsequently grow at different speeds (Figure 2a, step 3). The computer then dynamically monitors the bead positions (Figure 2a, step 4) and adjusts the forces, F_1 and F_2 (Figure 2a, step 5), according to the elastic coupling model (Figure 2b). For purely elastic couplers, the force difference across the two microtubules equals the tip separation, ($x_2 – x_1$), multiplied by the coupling stiffness (κ). When one microtubule grows more quickly than the other, tension on the leading (faster-growing) microtubule decreases and tension on the lagging (slower-growing) microtubule increases to maintain a constant total force on the pair, F_{TOT} (Supplemental Figure S3-1). For all the experiments described below, F_{TOT} = 8 pN, a value within the estimated physiological range of 0.4 to 8 pN per k-fiber microtubule (Nicklas, 1988; Powers et al., 2009).

Mechanical coupling coordinates microtubule pairs *in vitro*

To measure the effects of mechanical coupling, we recorded the growth of many pairs of microtubules coupled to a constant shared load (F_{TOT} = 8 pN) either through relatively soft springs, with κ = 1 pN·µm^{-1}, or through springs with five-fold greater stiffness, κ = 5 pN·µm^{-1}. These two stiffnesses span a range near the minimum elasticities estimated for mitotic chromosomes (Nicklas, 1983; Poirier et al., 2002), for pericentromeres (Chacon et al., 2014), and for elements of the kinetochore (Schwietert et al., 2022; Volkov et al., 2018). When coupled through soft springs (κ = 1 pN·µm^{-1}), microtubule pairs tended to grow at different rates and their tips often became separated by more than a micrometer (Figure 3a, left, and Figure S3-1, left). After 300 s, the average tip separation for soft-coupled pairs grew to 0.8 ± 0.2 µm (mean ± SEM from N = 10 pairs) (Figure 3b, left). When coupled through stiff springs (κ = 5 pN·µm^{-1}), growth speeds were better matched, and the microtubule tips remained closer together (Figure 3a, right, and Figure S3-1, right). The average tip separation for stiff-coupled pairs after 300 s was 0.25 ± 0.06 µm (mean ± SEM from N = 10 pairs) (Figure 3b, right), significantly lower than for soft-coupled pairs (p = 0.03 based on a Wilcoxon-Mann-Whitney two sample rank test).

Because the plus-ends of microtubules within k-fiber bundles are rarely separated by more than 0.8 µm from each other *in vivo* (O'Toole et al., 2020), we used Kaplan Meier survival analysis to ask how often the pairs of coupled microtubule tips in our experiments exceeded this threshold separation. Consistent with their lower average tip separation, stiff-coupled microtubule pairs were much less likely to exceed a separation of 0.8 µm than their soft-coupled counterparts (p = 0.01, log-rank test) (Figure 3c), which sometimes separated by 0.8 µm in as little as 60 s. Even after 400 s, more than 80% of the

149 stiff-coupled pairs had tip separations that remained below 0.8 µm, while fewer than half of the soft-
150 coupled pairs had tip separations below 0.8 µm. (Similar survival analyses using thresholds of 0.4, 0.6,
151 and 1.2 µm are provided in Supplemental Figure S6-2.)

152 Even at shorter time periods, the average behavior of soft- and stiff-coupled microtubule pairs
153 was distinct. During the first 100 s of growth, the average rate of tip separation for soft-coupled pairs
154 was 0.23 ± 0.04 µm·min^{-1} (mean ± SEM from N = 23 pairs), while the average rate of tip separation for
155 stiff-coupled pairs was only 0.14 ± 0.02 µm·min^{-1} (mean ± SEM from N = 26 pairs; p = 0.03 based on a
156 Wilcoxon-Mann-Whitney two sample rank test). Notably, the average rate of tip separation for stiff-
157 coupled microtubule pairs decreased as their average tip separation increased, suggesting they were
158 approaching a steady-state level of separation (Figure 3b, right). In contrast, the average rate of tip
159 separation for soft-coupled microtubule pairs remained approximately constant throughout the 400 s
160 measurement, suggesting that soft-coupled pairs would require more time to approach a steady state.
161 Altogether, these observations show that the growth of microtubule pairs can be tightly coordinated,
162 even over relatively short (< 100 s) timescales, by mechanically coupling their tips to a shared load
163 through couplers of sufficient stiffness.

164

165 **Models of microtubule growth variability and force sensitivity can be derived from recordings of**
166 **individual microtubules**

167 Coordination of microtubule growth can be thought of as the suppression of variability in
168 microtubule growth speed. Understanding how mechanical coupling suppresses variability requires a
169 realistic model of how the growth of individual microtubules varies over time and between
170 microtubules, as well as how growth behaviors are influenced by force. We therefore set out to create a
171 model of microtubule growth that explains both the variability between microtubules and the
172 suppression of their variability when they are coupled via a sufficiently stiff material.

173 To characterize the variability and force dependence of microtubule growth, we examined a
174 large set of 356 past recordings of individual microtubules growing under constant tension (force-clamp)
175 (Akiyoshi et al., 2010). This dataset was particularly relevant to our current studies because it was
176 recorded with an identical setup to our dual-trap experiments, except that each microtubule was grown
177 individually with a single laser trap exerting a constant level of tension (between 0.5 and 18 pN). Using
178 this dataset, we created two models derived from the natural variability of individual kinetochore-
179 attached microtubules and their average behaviors as a function of force. Below, we begin by briefly
180 describing a simple non-pausing model, which was developed first and served as a foundation for our
181 second, more successful pausing model. The pausing model reasonably explains our dual-trap results by
182 incorporating both stochastic pausing and intrinsic differences in microtubule growth speed.

183

184 **A simple non-pausing model predicts larger tip separations than measured *in vitro***

185 When averaged across time and across many individual microtubules, mean growth speed
186 increases exponentially with applied tension (Akiyoshi et al., 2010), such that

187 $$v_g = v_o * exp\left(\frac{F}{F_g}\right) \qquad [1]$$

188 where v_o represents the unloaded growth speed, F represents the applied tension, and F_g represents
189 the sensitivity with which the growth speed increases with tension. However, individual microtubules
190 show considerable variability around this mean behavior, with some microtubules remaining
191 persistently slower than others for many minutes (Figure 1a). In our first model, we adopted the simple
192 assumptions that this variability stems entirely from intrinsic differences in unloaded microtubule
193 growth speed, v_o, and that all microtubules have identical force-sensitivity (with F_g = 8.4 pN, based on
194 the exponential curve that best fit the mean growth speed-vs-force data (Akiyoshi et al., 2010)). In
195 principle, such static heterogeneity in growth speed might arise from persistent differences in
196 microtubule tip structure (Cleary & Hancock, 2021; Mahserejian et al., 2022; Rai et al., 2021) or from
197 variation in the numbers of protofilaments per microtubule (Chretien et al., 1992; Rai et al., 2021).

198 For each simulated microtubule, we randomly chose an individual growth speed measurement
199 from the force-clamp dataset (Akiyoshi et al., 2010), then extrapolated the microtubule's intrinsic
200 unloaded speed (v_o) from the chosen point (v_g, F) using equation [1] with F_g = 8.4 pN. The growth
201 speed of this simulated microtubule then followed the extrapolated curve as a function of force. To
202 simulate a pair of coupled microtubules, we made two such random draws from the dataset, defining
203 two distinct exponential (v_g-versus-F) relations for the two microtubules. (Bundles of three or more
204 microtubules could be simulated in the same manner by making additional draws.) We used a simple
205 Monte Carlo-based method (Gardner & Odde, 2010) to simulate traces of tip position versus time for
206 the pair. As in our dual-trap experiments, the simulated tip pairs were coupled with either soft or stiff
207 elastic springs to a constant shared load, F_{TOT} = 8 pN. Both the variability and force-dependence of
208 growth in the model were derived directly from the experimental force-clamp data, with no adjustable
209 ('free') parameters.

210 Despite its direct derivation from force-clamp data, the non-pausing model could not explain the
211 behavior of microtubule pairs measured in the dual-trap assay (Figure 4). Simulated microtubule pairs
212 developed much larger tip separations than real microtubule pairs over time, implying that this model
213 overestimates real microtubule variability. The simulated microtubule pairs showed especially poor
214 agreement with real microtubule pairs under the stiff-coupled condition (Figure 4c, red curves),
215 indicating that the non-pausing model also does not capture the degree to which real microtubules are
216 coordinated by mechanical coupling.

217

Microtubule growth is interrupted by stochastic, force-dependent pauses

Our simple non-pausing model lacked a notable behavior exhibited by microtubules that could influence their response to tension: Microtubule growth is frequently interrupted by stochastic pauses of varying durations, both in cells (Gaudenz et al., 2010; Sousa et al., 2007) and in purified tubulin systems (Mahserejian et al., 2022; Stumpff et al., 2012). Indeed, pauses recorded during our force-clamp (Figures 1a and S4-1b) and dual-trap assays (Figures 3a and S3-1) were frequent and often lasted tens of seconds. Presumably, these pauses occur because the configuration of the growing microtubule tip fluctuates and sometimes becomes transiently refractory to the incorporation of new tubulin subunits (Cleary & Hancock, 2021; Mahserejian et al., 2022). We hypothesized that entry and exit into the pause state might be force-dependent processes, and that pausing might therefore be a key aspect of microtubule force-sensitivity.

To test whether pause entry and exit rates vary with force, we reanalyzed the force-clamp dataset (Akiyoshi et al., 2010), applying a 2 s sliding window to identify intervals during each recording (N = 356) when the instantaneous growth speed fell to near-zero, indicative of a pause (Figure S5-1; see Materials and Methods for details about our pause marking procedure). The intervals in-between these pauses were designated as 'runs.' Distributions of run and pause durations were approximately exponential (Figure S5-2), consistent with a relatively simple two-state kinetic model of microtubule growth (Figure S5-1a), in which pause entry and exit are considered Poisson processes. For each force level, we estimated the pause entry and exit rates, k_{EN} and k_{EX}, by counting the total number of observed entrances into and exits out of pause and dividing by the total time spent in run and pause, respectively (Figure S5-1a).

This analysis revealed that tension delays pause entry and accelerates pause exit (Figure 5a). Both effects tend to decrease the time spent in the pause state for growing microtubule tips under high tension. In addition, the average growth speed during runs was accelerated by tension (Figure 5b). All three rates, pause entry, pause exit, and average growth speed during runs, were well-fit by single exponential functions of force (Figure 5; see Table 1 for fit parameters). These observations show that stochastic pausing during microtubule growth is force-dependent and imply that pausing kinetics will strongly influence the response of growing microtubules to mechanical coupling.

A pausing model can explain the variability between paired microtubule and their coordination by mechanical coupling

To examine how force-dependent pausing might affect the behavior of coupled microtubules, we created a second model in which growing microtubules switch stochastically between states of pause and run. Pause entry and exit were considered Poisson processes with kinetic rates dictated by the exponential fits of k_{EX} and k_{EN} versus force estimated from the force-clamp dataset (Figure 5a, dashed curves; Table 1). Intrinsic heterogeneity among microtubules was incorporated by randomly choosing an individual run speed measurement for each simulated microtubule from the force-clamp

255 dataset (i.e., by randomly choosing one point in Figure 5b). We then extrapolated the microtubule's
256 intrinsic unloaded run speed (v_{RUN}^{o}) from the chosen point (v_{RUN}, F) by assuming an exponential force-
257 dependence with sensitivity F_{RUN} = 14.8 pN (based on the dashed curve in Figure 5b; Table 1). The
258 growth speed during runs for this simulated microtubule then followed the extrapolated curve as a
259 function of force. We used a simple Monte Carlo-based method (again) to simulate traces of
260 microtubule tip position versus time. All model parameters were derived directly from the experimental
261 force-clamp data, with no adjustable ('free') parameters. As in our dual-trap experiments, simulated
262 microtubule tip pairs were coupled with either soft or stiff elastic springs to a constant shared load, F_{TOT}
263 = 8 pN. Simulations of individual microtubules growing under constant force closely resembled force-
264 clamp recordings of real microtubules *in vitro*. (Compare Figure S6-1 to Figure 1a.)

265 The pausing model of microtubule growth provided significantly better fits to our dual-trap data
266 than the non-pausing model. Like real microtubules in the dual-trap experiments, the simulated pairs of
267 tips tended to drift apart under soft-coupled conditions, while under stiff-coupled conditions they
268 stayed closer together (Figure 6a). After 300 s, the average tip separation for simulated soft-coupled
269 pairs grew to 0.79 ± 0.01 µm (mean ± SEM from N = 10,000 simulations), while simulated stiff-coupled
270 pairs had a lower average tip separation of 0.43 ± 0.005 µm (mean ± SEM from N = 10,000 simulations)
271 (Figure 6b), similar to the corresponding separations measured in dual-trap experiments (0.8 ± 0.2 µm
272 and 0.25 ± 0.06 µm, respectively). Simulated pairs of microtubule tips under stiff-coupled conditions
273 were also less likely to exceed a threshold separation of 0.8 µm (Figure 6c, dashed curves), similar to the
274 survival analyses of microtubule pairs measured with the dual-trap assay (Figure 6c, solid curves).
275 (Survival analyses of simulated microtubule pairs with threshold separations of 0.4, 0.6, and 1.2 µm also
276 resembled the survival analyses of microtubule pairs measured with the dual-trap assay. See Figure S6-
277 2.) In addition, the pausing model scored better than the non-pausing model when we used probability
278 to compare simulated to *in vitro* measurements (Figure S6-4). (To quantify the variability due to
279 stochastic pausing alone, we also compared the pausing model to a version in which we assumed that
280 microtubules were intrinsically identical ('ergodic'). The low variability predicted by this model (Figure
281 S6-3), particularly under the soft-coupled condition, indicates that stochastic pausing alone is
282 insufficient to generate the large and persistent differences in growth speed exhibited by real
283 microtubules). Overall, the strong agreement between the pausing model and the dual-trap recordings
284 suggests that mechanical coupling coordinates microtubule growth in at least two distinct ways: first, by
285 counteracting persistent (intrinsic) differences in microtubule growth speed, and second, by selectively
286 suppressing stochastic pausing in the lagging tip relative to the leading tip.

287

288 **Discussion**

289 Our work demonstrates the effectiveness of mechanical coupling for coordinating the growth of
290 microtubules and helps explain how numerous filaments within a k-fiber bundle can be tightly regulated
291 to grow in near-perfect unison. Using our dual-trap assay, we found that pairs of microtubule tips
292 growing *in vitro* are kept in close proximity when sharing a single load through a coupling material of
293 sufficient stiffness. Tip pairs in our experiments were kept within a fraction of a micrometer by couplers
294 of only κ = 5 pN·µm^{-1}, a modest stiffness within the ranges reported for elements of the kinetochore

295 (Schwietert et al., 2022; Volkov et al., 2018), pericentromeric chromatin (Chacon et al., 2014), and
296 mitotic chromosomes (Nicklas, 1983; Poirier et al., 2002). Because the kinetochore, its underlying
297 centromeric chromatin, and k-fiber plus-ends appear to deform with each other to maintain close
298 contacts *in vivo* (O'Toole et al., 2020), the plus-ends presumably exert forces on each other through a
299 composite material composed of both kinetochore and chromatin. We propose that this mechanical
300 coupling is a major coordinating influence on plus-end growth dynamics within k-fiber bundles.

301 A variety of microtubule-modifying proteins are also implicated in regulating k-fiber dynamics
302 (reviewed in (Ou & Scholey, 2022) and (Amin et al., 2019)). These biochemical factors must work in
303 concert with mechanical effects, and we suggest that the two classes of mechanisms probably operate
304 over different length- and timescales. Certain tip-tracking proteins capable of influencing microtubule
305 dynamics are enriched at growing k-fiber ends specifically near kinetochores that are moving anti-
306 poleward (Amaro et al., 2010; Castrogiovanni et al., 2021; Tirnauer et al., 2002). Various kinesins are
307 known to regulate the size of the metaphase spindle (Goshima et al., 2005; Neahring et al., 2021), to
308 influence k-fiber dynamics (Maiato, Fairley, et al., 2003; Rizk et al., 2009; Stumpff et al., 2012;
309 Wordeman et al., 2007), and to alter microtubule dynamics *in vitro* in a length-dependent manner
310 (Varga et al., 2006). However, it is unclear whether the specific enrichment of such microtubule-
311 modulators on longer or faster-growing tips could occur quickly enough and with enough selectivity to
312 slow the growth of a single tip that has grown ahead of its neighbors by only a fraction of a micrometer,
313 as required for tight coordination within a k-fiber. On the other hand, mechanical forces would be
314 transmitted essentially instantaneously between neighboring tips through local deformations of the
315 material through which the tips are coupled. Therefore, mechanical coupling could account for the
316 rapid, sub-micron responses required to coordinate microtubule tips within a k-fiber, while microtubule-
317 modifiers and spindle-wide phenomena, like polar ejection forces and poleward flux, are likely to help
318 set overall k-fiber length (Risteski et al., 2021).

319 We found that tension accelerates microtubule growth not only by directly increasing growth speed,
320 but also by decreasing time spent in pause. More specifically, tension reduced the rate at which growing
321 tips entered a pause state. This finding implies that pause entry is associated with movement of tension-
322 bearing elements at the tip toward the minus end, opposite the direction of applied force and therefore
323 inhibited by the force. Tension also increased the rate at which paused tips resumed growth, which
324 implies that pause exit is associated with movement toward the plus-end, in the same direction as the
325 applied force and therefore assisted by the force. An attractive explanation for these observations is
326 that pauses occur when newly added tubulin dimers at a growing tip adopt curved structures (McIntosh
327 et al., 2018) that disfavor lateral bonding and that tension helps to straighten these curved structures,
328 thereby accelerating lateral bond formation and favoring growth (Cleary & Hancock, 2021).

329 We derived a model of microtubule growth with no free parameters, based on constant-force
330 recordings of individual microtubules (from (Akiyoshi et al., 2010)), and found that a combination of
331 stochastic, force-dependent pausing and intrinsic differences in microtubule growth speed explained
332 both the variability and the coordination measured in our dual laser trap assay. The necessity of
333 including microtubules with different intrinsic growth speeds for our model's success implies structural
334 heterogeneity in the growing tips that must persist for many minutes, even as thousands of tubulin
335 subunits are being added. In principle, these persistent differences might arise from different or
336 mismatched protofilament numbers (Chretien et al., 1992; Rai et al., 2021) or the accumulation of other
337 lattice defects (Wieczorek et al., 2015) that result in varying degrees of tip taper (Coombes et al., 2013)
338 (or tip "raggedness" (Brouhard & Rice, 2018)) which are more or less conducive to microtubule growth.

For technical reasons, we focused the present work exclusively on microtubule tips in a state of net growth. However, coordination of k-fiber microtubules *in vivo* presumably also requires tight regulation of tip shortening speeds and rates of switching between growth and shortening (i.e., 'catastrophe' and 'rescue' rates). These will be more difficult to study with our dual-trap assay because switch events are stochastic and episodes of shortening are observed less frequently than episodes of growth under our assay conditions. Nevertheless, the dual-trap approach can be used in the future (potentially with a cutting laser to sever the microtubule tips to induce shortening (Driver et al., 2017; Murray et al., 2022)) to study how mechanical coupling affects microtubule pairs in which one or both filaments are shortening, as well as switch rates between shortening and growth. Our dual-trap approach can also be adapted to examine mechanical coupling through materials with complex mechanical properties, such as viscoelasticity and strain-stiffening (Cojoc et al., 2016; Schwietert et al., 2022). The effect of mechanical coupling on pairs of processive motor proteins (Holzbaur & Goldman, 2010) or pairs of dynamic actin filaments linked to a shared load (Garner & Theriot, 2022) can also be studied with the dual-trap approach. While extending our *in vitro* laser trap methods to more than two microtubules would be impractical, our model is easily extended to explore mechanical coordination within k-fibers of three or more microtubules, as found in the spindles of many eukaryotes. Overall, our work demonstrates that mechanical coupling is a feasible mechanism that could coordinate k-fiber microtubules and maintain their synchronous growth in the mitotic spindle.

Funding and Acknowledgements

We are grateful for feedback and critical reading of the manuscript from members of the Biggins, Asbury, and Trisha Davis laboratories.

This work was supported by a Packard Fellowship 2006-30521 (to C.L. Asbury), National Institutes of Health grants R01GM079373, P01GM105537, and R35GM134842 (to C.L. Asbury) and R01GM064386 (to S. Biggins), and by the Genomics and Scientific Imaging and the Proteomics and Metabolomics Shared Resources of the Fred Hutchinson/University of Washington Cancer Consortium (P30 CA015704). S. Biggins is an investigator of the Howard Hughes Medical Institute. Research reported in this publication was also supported by the National Institute of General Medical Sciences of the National Institutes of Health under Award Number T32GM008268 (to B.K. Leeds).

Author contributions: Conceptualization (C.L. Asbury, B.K. Leeds), data curation (B.K. Leeds, Y. Liu), formal analysis (B.K. Leeds, Y. Liu), funding acquisition (C.L. Asbury, S. Biggins, B.K. Leeds) investigation (B.K. Leeds, K.F. Kostello, C.L. Asbury), project administration (C.L. Asbury), resources (C.L. Asbury, S. Biggins), software (B.K. Leeds, C.L. Asbury, Y. Liu), supervision (C.L. Asbury, S. Biggins, B.K. Leeds), validation (B.K. Leeds, K.F. Kostello, Y. Liu, C.L. Asbury), visualization (B.K. Leeds, C.L. Asbury, K.F. Kostello, Y. Liu), writing–original draft (B.K. Leeds, C.L. Asbury), writing–review and editing (B.K. Leeds, C.L Asbury, K.F. Kostello, S. Biggins).

377 **Methods**

378 **Spring-coupler model**

379 For both *in vitro* and *in silico* experiments, the force on each microtubule plus-end was dictated by a
380 model in which plus-ends were coupled to a shared "kinetochore" via simple Hookean springs of
381 identical stiffnesses (Figure 2b). Because k-fibers grow relatively slowly in cells (Khodjakov et al., 1996;
382 Skibbens et al., 1993; Stumpff et al., 2012), we neglect viscous drag such that the sum of the forces on
383 individual k-fiber tips equals F_{TOT}. Microtubule pairs were considered to grow along a shared 1D axis.
384 Microtubules were assumed to be incompressible because microtubules have high axial stiffness
385 (Howard, 2001; Kis et al., 2002; Pampaloni et al., 2006) and are cross-linked in bundles (O'Toole et al.,
386 2020), thus forming the structural support required to maintain mitotic spindle integrity. Microtubules
387 were considered stationary except at the plus-end, so that only growth or shortening at the plus-end
388 affected plus-end position.

389

390 **Kinetochore purification**

391 Native kinetochore particles were purified from asynchronously grown *S. cerevisiae* SBY8253 cells
392 (Genotype: MATa DSN1-6His-3Flag:URA3) grown in YPD medium (2% glucose) by modifying previous
393 protocols (Akiyoshi et al., 2010; Miller et al., 2016). Protein lysates were prepared using a Freezer Mill
394 (SPEX SamplePrep) submerged in liquid nitrogen. Lysed cells were resuspended in buffer H (25 mM
395 Hepes, pH 8.0, 2 mM MgCl2, 0.1 mM EDTA, 0.5 mM EGTA, 0.1% NP-40, 15% glycerol, and 150 mM KCl)
396 containing phosphatase inhibitors (0.1 mM Na-orthovanadate, 0.2 µM microcystin, 2 mM β-
397 glycerophosphate, 1 mM Na pyrophosphate, and 5 mM NaF) and protease inhibitors (20 µg/ml
398 leupeptin, 20 µg/ml pepstatin A, 20 µg/ml chymostatin, and 200 µM PMSF). Lysates were
399 ultracentrifuged at 98,500 g for 90 min at 4°C. Protein G Dynabeads (Invitrogen) were conjugated with
400 an α-FLAG antibody (Sigma-Aldrich), and immunoprecipitation of Dsn1-6His-3Flag was performed at 4°C
401 for 3 h. Beads were washed once with lysis buffer containing 2 mM DTT and protease inhibitors, three
402 times with lysis buffer with protease inhibitors, and once in lysis buffer without inhibitors, and
403 kinetochore particles were eluted by gentle agitation of beads in elution buffer (buffer H + 0.5 mg/ml
404 3FLAG Peptide [Sigma-Aldrich]) for 30 min at room temperature.

405

406 **Bead functionalization and slide preparation for laser trap experiments**

407 To functionalize laser trapping beads with native kinetochore particles, streptavidin-coated polystyrene
408 beads (0.44 µm in diameter, Spherotech) were incubated with biotinylated anti-5His antibodies (Qiagen)
409 and stored for up to 6 months with continuous rotation at 4°C in BRB80 (80 mM Pipes, 1 mM $MgCl_2$, and
410 1 mM EGTA, pH 6.9) supplemented with 8 mg*mL^{-1} bovine serum albumin and 1 mM DTT. Before each
411 experiment, functionalized beads were sonicated for two minutes and decorated with kinetochore
412 particles by incubating 6 pM anti-5His beads for 1-2 hours at 4°C with purified kinetochore material,
413 corresponding to concentrations of Dsn1-His-Flag between 1.5 and 4 nM, well within the single-
414 kinetochore-particle condition described in (Akiyoshi et al., 2010).

415 Each flow chamber (~5-10 µL in volume) was constructed by placing two parallel strips of double-stick
416 tape between a glass slide and a KOH- or plasma-cleaned coverslip. Immediately before every
417 experiment, two flow chambers were each functionalized as follows. First, flow chambers were
418 incubated with 10 µL of 10 mg*mL^{-1} biotinylated bovine serum albumin (Vector Laboratories) for 15
419 minutes at room temperature. Chambers were then washed with 100 µL BRB80. Next, 20 µL of 333
420 mg*mL^{-1} avidin DN (Vector Laboratories) in BRB80 was added to the chamber and incubated for 3
421 minutes before washing again with 100 µL BRB80. Chambers were then incubated for 5 minutes with
422 GMPCPP-stabilized biotinylated microtubule seeds warmed for 5-10 minutes in BRB80. Next, chambers
423 were washed with 100 µL of growth buffer (1 mM GTP, 1 mg*mL^{-1} K-casein, and .08 mg*mL^{-1}
424 biotinylated bovine serum albumin in BRB80). Finally, chambers were incubated with kinetochore-
425 decorated beads diluted approximately 8-fold into growth buffer augmented with 1.5 mg*mL^{-1} purified
426 bovine brain tubulin and an oxygen scavenging system (1 mM DTT, 500 µg*mL^{-1} glucose oxidase, 60
427 µg*mL^{-1} catalase, and 25 mM glucose). The flow chamber exit and entrance were then sealed with nail
428 polish and used for experiments at 23°C for up to 2 hours.

429

430 **Performing the dual-trap assay**

431 Laser trap experiments were performed using two custom-built instruments based on commercial
432 inverted microscopes (Nikon; TE2000U) modified to each incorporate a trapping laser (Spectra-Physics;
433 J20I-BL-106C-NSI), a computer-controlled piezo specimen stage (Physik Instrumente; P-517.3CL), and a
434 position-sensitive photodetector (Pacific Silicon Sensor; DL100-7-PCBA2). See (Franck et al., 2010) for
435 details regarding instrument setup and calibration.

436 The dual-trap assay was modified from previous force-clamp protocols (Akiyoshi et al., 2010; Franck et
437 al., 2010; Miller et al., 2016) and maintained constant total force on two bead-laser trap systems, rather
438 than one (Figure 2a). Both lasers were controlled by a single computer, which adjusted the force on each
439 bead to maintain force equilibrium on the modeled "kinetochore" given the measured bead positions
440 (Figure 2b). We approximated the bead position as the microtubule tip position, since kinetochore-
441 decorated beads are known to track with microtubule plus-ends under tensions between 0.5 and 18 pN
442 (Akiyoshi et al., 2010; Asbury et al., 2006; Franck et al., 2010; Miller et al., 2016; Powers et al., 2009; Tien
443 et al., 2010) and the elastic linker connecting the microtubule plus-end to the bead stays the same
444 length under relatively stable force conditions. We recorded the position of a free bead using each laser-
445 trap at the start of each 2-hour experiment, and as necessary between recordings, to calibrate the laser
446 trap's zero-force position. Feedback to exert precisely the amount of force dictated by the relative bead
447 positions and the spring-coupler model was implemented with custom LabView software (National
448 Instruments). Bead-trap separation was sampled at 40 kHz, while stage position was updated at 50 Hz.
449 Bead and stage position data were decimated to 200 Hz before storing to disk.

450 LabView software to perform force-clamp experiments is available at
451 https://github.com/casbury69/laser-trap-control-and-data-acquisition and the LabView software to
452 perform dual-trap experiments is available at https://github.com/casbury69/dual-trap-control-and-data-
453 acquisition.

454

455 **Analyzing dual-trap recordings**

456 We analyzed recordings from the dual-trap assay using custom software made in Igor Pro 9
457 (Wavemetrics). First, by hand, we marked the beginning and end of recorded segments in which both
458 microtubules were growing and separated these episodes into individual recordings. We then calculated
459 the tip separation between coupled microtubules for each excised recording by taking the absolute
460 value of the difference in position at 1 s intervals from 0 to 400 s. For each recording, total force on the
461 microtubule pair was computed by adding the force on both microtubules together at 0.005 s intervals
462 (Fig. S3-1).

463 To calculate the speed of tip separation, we fit the first 100 s to a line with the Levenberg-Marquardt
464 method. Uncertainties in tip separation speed were estimated from residuals as described in (Press et
465 al.).

466 SEMs for microtubule pair tip separation measured using the dual-trap assay (Figure 3b) were calculated
467 at 1 s intervals after the recording began using the following equation:

468 $$SEM_{tip\ sep}(t) = \frac{\sigma_t}{\sqrt{N_t}}$$

469 where σ_t is the standard deviation of the tip separations at t seconds and N_t is the number of
470 microtubule pairs which were still growing and tip-attached to a bead at t seconds.

471 Download 'Dual-trap viewer.pxp' at https://github.com/casbury69/dual-trap-data-analysis to view
472 position- and force-versus-time curves for each of the dual-trap recordings analyzed in this work. See
473 also 'Dual-trap anlaysis.txt' at https://github.com/casbury69/dual-trap-data-analysis for the software
474 used to analyze dual-trap recordings.

475

476 **Creating Kaplan-Meier survival curves**

477 Kaplan-Meier survival curves for both simulated and *in vitro* microtubule pairs (Figure 3c, Figure 4c,
478 Figure 6c, Figure S6-2, and Figure S6-3c) were calculated at 1 s intervals after the recording began using
479 the following equation:

480 $$S(t) = \prod_{j=0}^{t} \frac{n_j - d_j}{n_j}$$

481 where $S(t)$ is the Kaplan-Meier survival probability at t seconds, t is the number of Kaplan-Meier
482 estimates made between time 0 and t seconds, n_j is the number of microtubule pairs still growing, tip-
483 attached to a bead, and within the threshold tip separation at j seconds, and d_j is the number of
484 microtubule pairs that exceeded the threshold tip separation (0.4, 0.6, 0.8, or 1.2 µm) between time $j -$
485 1 and j seconds.

SEMs for Kaplan-Meier survival plots estimated using the dual-trap assay (Figure 3c and Figure S6-2) were calculated at 1 s intervals after the recording began using the following equation:

$$SEM_{survival}(t) = S(t) * \sqrt{\sum_{j=1}^{t} \frac{d_j}{n_j(n_j - d_j)}}$$

where $S(t)$ is the Kaplan-Meier survival probability at t seconds, t is the number of Kaplan-Meier estimates made between time 0 and t seconds, d_j is the number of microtubule pairs that exceeded the threshold tip separation (0.4, 0.6, 0.8, or 1.2 µm) between time $j - 1$ and j seconds, and n_j is the number of microtubule pairs still growing, tip-attached to a bead, and within the threshold tip separation at j seconds.

Segmenting constant force traces into periods of run and pause

To estimate pause entrance and exit rates as a function of force, we segmented N = 356 recordings of growing microtubules under constant force (from (Akiyoshi et al., 2010)) into pauses and fast growth ('runs,' Figure S5-1a and b). First, we estimated the instantaneous growth speed over the entirety of each recording to be the slope of the best fit line for a sliding 2 s window (Figure S5-1c). Next, we defined a unique threshold between pause and run for each recording by assembling a histogram of growth speeds throughout the recording and fitting that histogram with a sum of between two and six Gaussian peaks. We centered one Gaussian at or near 0 µm·min^{-1} and defined it as the 'pause' peak. Fitting the growth speed histograms to Gaussian peaks was performed using the 'Multipeak fitting' package in Igor Pro 9. The intersection of the pause peak and the Gaussian with the next highest mean growth speed was identified for each individual recording and defined as the threshold to distinguish pauses and runs for that recording.

To reduce the impact of high-frequency noise, we excluded pauses and runs that lasted less than 1 s. If the instantaneous growth speed fell below that recording's predefined threshold for at least 1 s, the microtubule was considered to have paused. If the instantaneous growth speed fell below the threshold for less than 1 s, the short interval was combined with the run intervals before and after to make a single run. Likewise, if the instantaneous growth speed exceeded the threshold for at least 1 s, the microtubule was considered to be in run. If the instantaneous growth speed exceeded the threshold for less than 1 s, the short interval was combined with the pause intervals before and after to make a single pause. If the defined threshold was never crossed, the recording was considered a single run interval.

Download 'Force-clamp viewer.pxp' at https://github.com/casbury69/laser-trap-data-viewer to view position- and velocity-versus time curves for each force-clamp recording analyzed in this work, as well as how pauses were marked for each recording. This file also includes additional shortening events which were not studied here. See also 'Force-clamp viewer.txt' at https://github.com/casbury69/laser-trap-data-viewer for the software used to distinguish pauses from runs.

Quantifying growth speed during runs for individual recordings

For each pause-based model that we considered, microtubule growth speed during runs was assumed to be time-invariant under constant force. Thus, we made the same assumption when we quantified the growth speed during runs of individual microtubules *in vitro*, and calculated a unique growth speed during runs for each recording (dots in Figure 5b). The growth speed during each run interval was calculated by averaging together the instantaneous growth speeds comprising that interval, measured with the 2 s sliding window described above. We calculated the overall growth speed during runs for a single microtubule by averaging together the growth speed of all contained run intervals, weighted by the duration of that interval, such that:

$$v_{run} = \frac{\sum v_i * t_i}{T}$$

where v_{run} is the overall growth speed during runs for a particular recording, v_i is the growth speed for the ith run interval, t_i is the duration of the ith run interval, and T is the total time spent in the run state.

Quantifying the force dependence of pause entrance rates, exit rates and growth speed

To calculate average pause exit rates, entrance rates, and growth speeds as a function of force we binned each recording by the constant tensile force to which the microtubule was subjected (Figure 5). For consistency, we used the same seven force bins used by (Akiyoshi et al., 2010) (see Table 2 for bin boundaries). For both the pause entrance and exit rate, we excluded the highest force bin from our analysis because of low statistics. For each force bin, we calculated the mean pause entrance and exit rate by counting the number of times microtubules in that force bin entered and exited pause and dividing by the total time microtubules in that bin spent in run and pause, respectively (Figure S5-1a). Error bars in the y-direction represent counting uncertainties, calculated with the equation:

$$SEM_{rate}(i) = \frac{k_i}{\sqrt{N_i}}$$

where k_i is the rate of pause entrance or exit for the ith force bin, and N_i is the number of pause entrances or exits in the recordings in the ith bin (N = 387 to 3502 pause entrances and N = 378 to 3501 pause exits per bin, see Table 2 for the number of pause entrances and exits by bin). Error bars in the x-direction represent standard deviations of forces for the recordings in each bin.

We found the mean growth speed during runs for each force bin by averaging together the growth speed during runs for all the recordings in that bin. Error bars in the y-direction represent the SEMs of growth speeds, calculated with the equation:

$$SEM_{run\ speed}(i) = \frac{\sigma_i}{\sqrt{N_i}}$$

where σ_i is the standard deviation of the growth speeds during runs, averaged over each recording, for the ith force bin, and N_i is the number of recordings in the ith bin (N = 9 to 85 recordings per bin, see

554 Table 2 for the number of recordings by bin). Once again, error bars in the x-direction represent the
555 standard deviations of forces for the recordings in each bin. Fit lines for pause exit and entrance rates
556 and growth speed were calculated with Levenberg-Marquardt least-squares method (Press et al.).

557

558 **Simulating pairs of growing microtubules**

559 Simulated recordings using each model followed the same general procedure. For simulations in which
560 the growth or run speed was different between microtubules (both non-ergodic models), the 'unloaded'
561 growth or run speed was drawn from a distribution of measured growth or run speeds as described in
562 the results section. For the non-ergodic pausing model, intrinsic unloaded run speeds ($v_{intrinsic}$) of
563 more than 30 nm/s were considered outliers and excluded from the distribution. For microtubules
564 simulated with the ergodic pausing model, both microtubules had the same growth speed during runs,
565 based on the equation and parameters for v_{run} in Table 1. Each simulation began with both
566 microtubules growing (in run, for pause-based models) from the same position under the same tensile
567 force. As microtubules stochastically grew or paused, the tensile force on each microtubule evolved
568 according to the spring-coupler model, just like they did in the dual-trap assay. As the force changed,
569 depending on the model type, the growth or run speed changed according to exponential relationships
570 with force estimated from (Akiyoshi et al., 2010) (Table 1).

571 A modified Gillespie algorithm was used to implement stochastic microtubule events: pause entrance
572 and exit, detachment from the kinetochore, switches into shortening (catastrophe), and other event
573 interruptions. Each of these event rates were assumed independent Poisson processes and were derived
574 directly from the data summarized in (Akiyoshi et al., 2010). Each microtubule was assumed to have
575 identical rates for all stochastic events, given the same external force. Detachment and catastrophe
576 rates were calculated using the exponential relationships as a function of force estimated by (Akiyoshi et
577 al., 2010).The rate of interruption by other events was also estimated from these force-clamp recordings
578 but was force-independent. For simulations that included pausing, rates of pause entrance and exit
579 were calculated from the fit equations in Table 1 (fit lines in Figure 5).

580 Because detachment, catastrophe, and pause rates are force-dependent, they can only be approximated
581 as Poisson (time-invariant) rates for short time intervals over which the force on the tip is relatively
582 constant. Consequently, we imposed a maximum timestep of no greater than 1 s for each simulation. If
583 the timestep chosen by our Gillespie algorithm exceeded the maximum timestep, no event occurred and
584 the microtubule continued growing during that 1 s interval. All simulations were performed using
585 custom software in Igor Pro 9 (Wavemetrics).

586 Download 'Dual-trap simulations.pxp' at https://github.com/casbury69/simulations-of-coupled-
587 microtubules to run dual-trap simulations as described in the results and see 'Dual-trap simulator.txt' at
588 https://github.com/casbury69/simulations-of-coupled-microtubules for the code used to run these
589 simulations.

590

591 **Comparing pausing and non-pausing models with simple probability**

To evaluate whether the pausing or non-pausing model was more likely given our dual-trap measurements, we compared histograms of tip separations at 100 and 200 s after the start of the recording or simulation (Figure S6-4). We used 0.1 µm bins for both simulated and dual-trap data and normalized all histograms to have an area of 1.

We calculated the likelihood that simulations performed using the pausing and non-pausing models would produce each *in vitro* tip separation:

$$L_{measurement} = w_{bin} * P_{normalized}$$

where w_{bin} is the bin width of the tip separation histogram (0.1 µm) and $P_{normalized}$ is the normalized probability of the given model at the measured tip separation (y-values of the dashed lines in Figure S6-4).

To compare the overall likelihood that the pausing and non-pausing simulations would produce all the tip separations measured *in vitro*, we multiplied together the likelihoods of each measurement for a given model at a given coupler stiffness and at a given time point. We calculated the log likelihood by taking the base 10 logarithm of each probability (reported in the right-hand column of each table in Figure S6-4).

Statistical analysis

All statistical analysis was performed using custom software written in Igor Pro 9 (Wavemetrics).

We calculated p-values to determine whether survival curves of stiff-coupled and soft-coupled *in vitro* microtubule pairs were statistically different for each threshold tip separation using a log-rank test. For each survival curve, at 1 s intervals after the recording began, we calculated an expected value using the following equation:

$$E(t) = \frac{n_t}{n_{tot}}(d_{tot})$$

where n_t is the number of microtubule pairs comprising one survival curve that are still growing, tip-attached to a bead, and within the threshold tip separation at t seconds, n_{tot} is the total number of microtubule pairs comprising both survival curves being compared that are still growing, tip-attached to a bead, and within the threshold tip separation at t seconds, and d_{tot} is the total number of microtubule pairs that exceeded the threshold tip separation between time $t-1$ and t seconds for both survival curves being compared. Expected values for each pair of survival curves were used to calculate a chi-square value for each tip separation threshold using the following equation:

$$\chi^2 = \sum_{j=1}^{2} \frac{\left(\sum_{t=1}^{T} S_j(t) - \sum_{t=1}^{T} E_j(t)\right)^2}{\sum_{t=1}^{T} E_j(t)}$$

where T is the total number of timepoints (400, in all cases), $S_j(t)$ is the Kaplan-Meier survival probability of curve j at time t, and $E_j(t)$ is the expected value of Kaplan-Meier survival curve j at time t. A chi-square table was then used to estimate the p-value for each tip separation threshold.

To determine whether tip separation and tip separation speed between soft and stiff couplers were statistically significant, we calculated p-values with a Wilcoxon-Mann-Whitney two sample rank test using built-in Igor Pro software (Cheung & Klotz, 1997; Klotz, 2006; Streitberg & Rohmel, 1986; Zar, 1999).

631 **Figures**

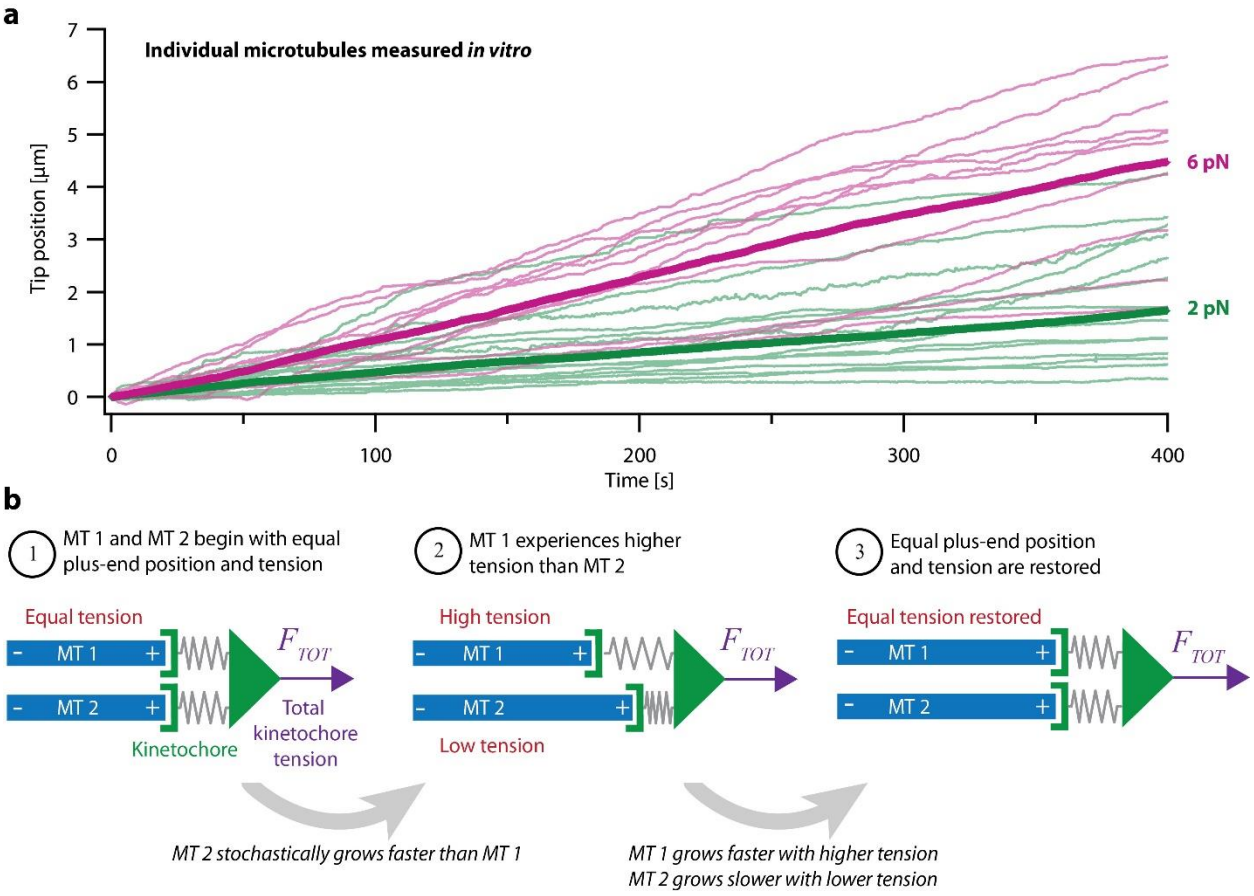

632
633

634 **Figure 1. Intrinsic variability in microtubule growth could be coordinated by mechanical coupling.** (**a**) Microtubules (MTs)
635 grow at intrinsically variable rates that increase with force, on average. Example recordings show plus-end position versus time
636 for individual growing microtubules subject to a constant tensile force of either 2 or 6 pN (thin green or magenta traces,
637 respectively). At each force, 10 to 14 example recordings are shown, together with the mean position versus time (thick traces,
638 computed from N = 25 or N = 10 individual recordings at 2 or 6 pN, respectively). Individual traces are from (Akiyoshi et al.,
639 2010). (**b**) Mechanism by which mechanical coupling could coordinate growing microtubules. In this example, two microtubules
640 share a total force, F_{TOT}, through two spring-like connections to their plus-ends. If one microtubule stochastically lags behind, it
641 will experience more tension than the leading microtubule due to differential stretching of their spring-connections. Because
642 tension tends to accelerate plus-end growth (as illustrated in panel a), the higher tension will tend to accelerate the growth of
643 the lagging microtubule, causing it to catch up.

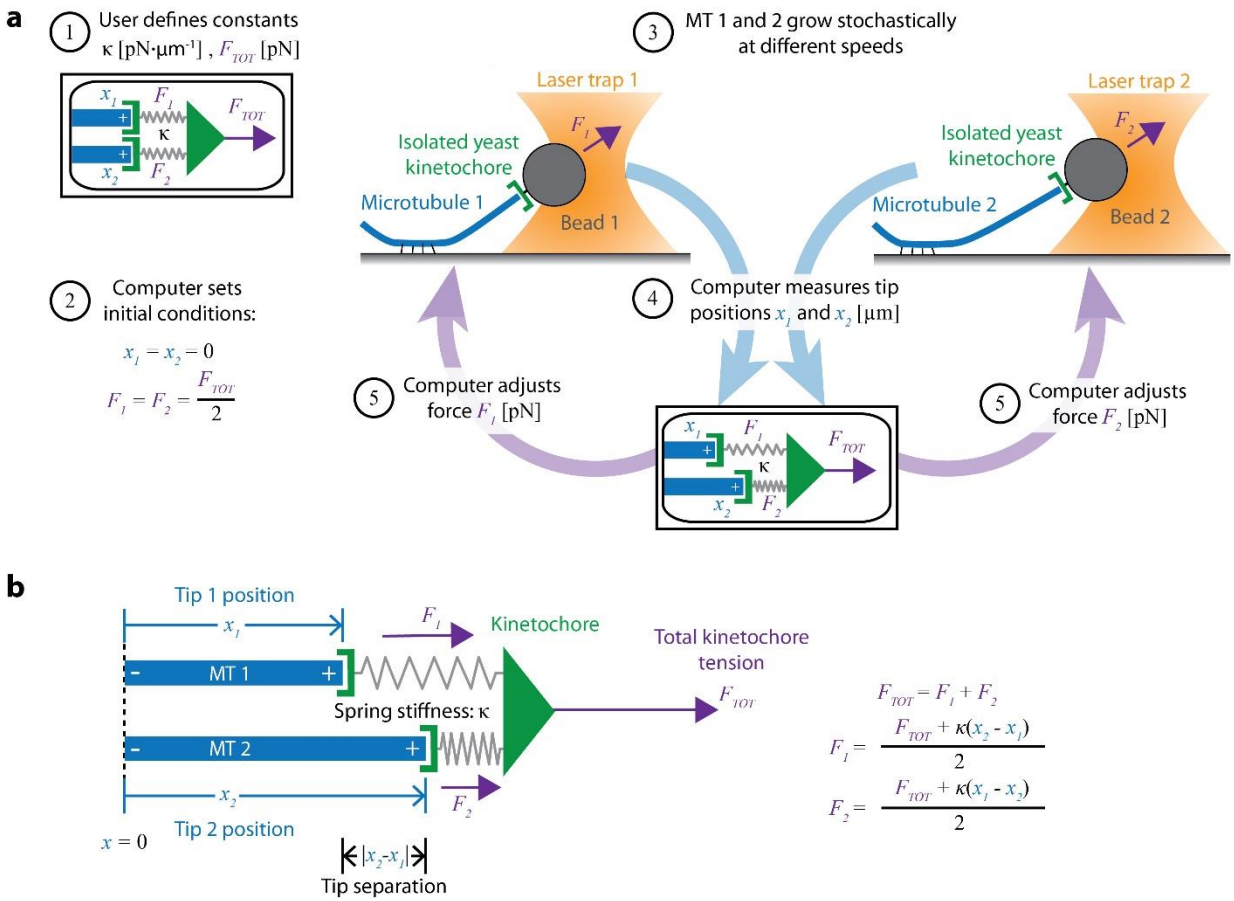

Figure 2. Dual-trap assay to measure the coordination of two real microtubules *in vitro* coupled together by simulated spring-like connections to a shared tensile load. (**a**) Schematic of the dual-trap assay, which measures the effects of the spring-coupler model (detailed in b) on real microtubules (MTs) growing *in vitro*. Two dynamic microtubules are grown from seeds anchored to two separate coverslips on two separate stages, each with their own microscope and laser trap. Each laser trap applies tension to its respective microtubule plus-end via a bead decorated with isolated yeast kinetochores, and each tension is adjusted dynamically under feedback control by a shared computer. Initially (steps 1 and 2), microtubule plus-ends are considered to have the same position ($x_1 = x_2 = 0$) so that each bears half of the total user-input tension (F_{TOT}). Over time, as microtubules grow at different rates (step 3), the computer dynamically adjusts the tension on each microtubule according to the spring-coupler model (steps 4 and 5), so that the higher the tip separation ($|x_1 - x_2|$) and stiffness (κ), the larger the difference in tension between the two microtubules. (**b**) Spring-coupler model used to represent the physical connection between two microtubule plus-ends via a kinetochore. Both springs have identical stiffnesses (κ). The kinetochore is assumed to be in force equilibrium such that the sum of the spring forces is equal to the total external force, F_{TOT}, which is kept constant in the current study.

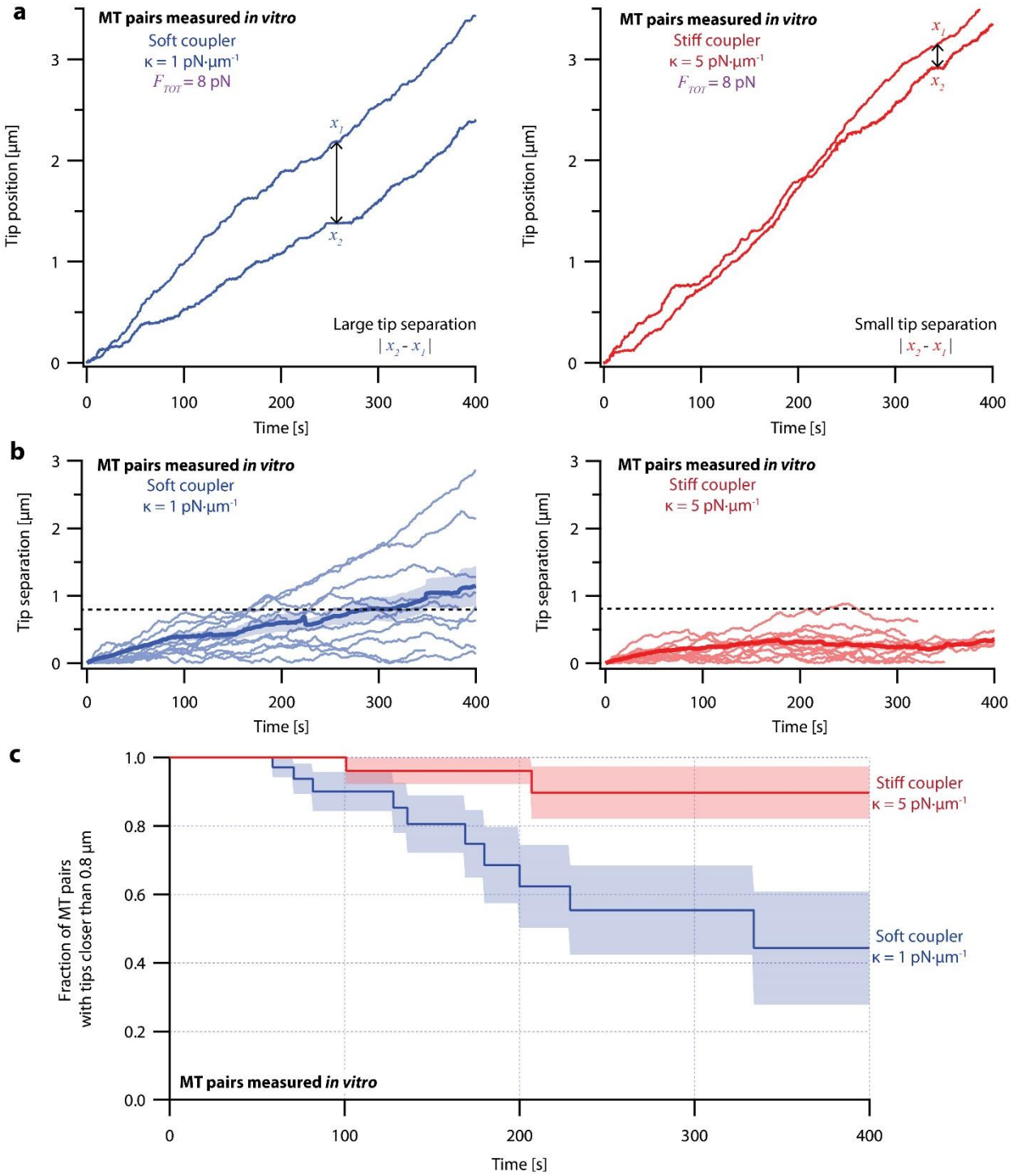

Figure 3. Microtubule pairs growing *in vitro* are coordinated by mechanical coupling. (**a**) Example dual-trap assay recordings showing real microtubule (MT) plus-end positions over time for representative microtubule pairs coupled via soft (1 pN·µm^{-1}, left) or stiff (5 pN·µm^{-1}, right) simulated spring-couplers. All dual-trap data was recorded with F_{TOT} = 8 pN. (**b**) Tip separation ($|x_1 - x_2|$) between microtubule plus-end pairs that were coupled with either soft (left) or stiff (right) simulated spring-couplers over 400 s of growth. Light colors show tip separations for 10 individual microtubule pairs with each coupler stiffness, while dark colors show mean tip separation for all recorded pairs (N = 50 and N = 43 recordings with soft and stiff couplers, respectively). (**c**) Fraction of microtubule pairs whose plus-ends remained within 0.8 µm of each other over time. (In other words, the fraction of pairs at any given time whose tip separation had not exceeded the dashed line in (b).) Shaded regions in (b) and (c) show SEMs from N = 50 and N = 43 recordings with soft and stiff couplers, respectively.

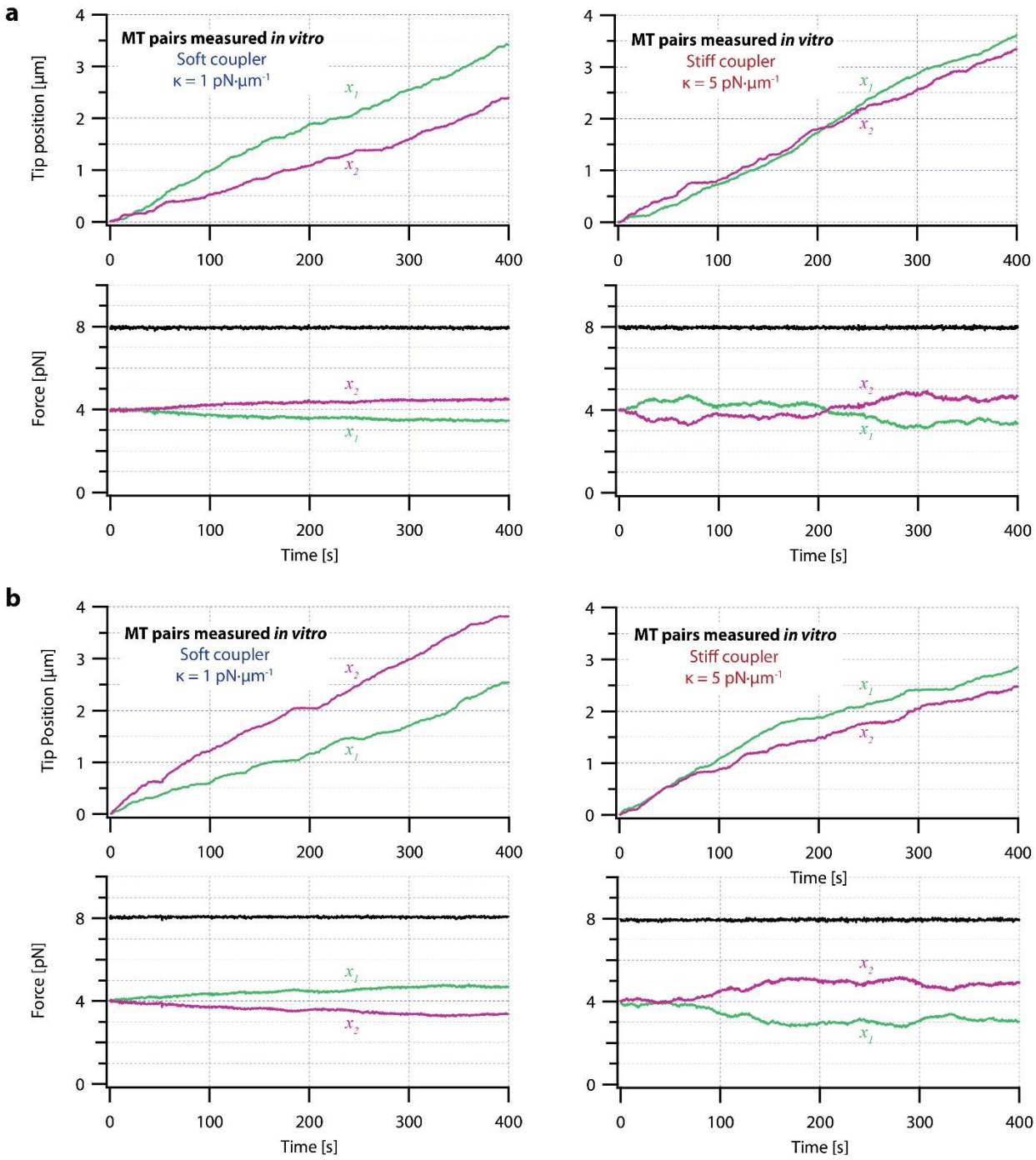

Figure S3-1. Additional dual-trap assay recordings showing tip positions and forces on pairs of growing microtubules. (**a**) Example dual-trap assay recordings showing real microtubule (MT) plus-end positions (top) and forces (bottom) plotted against time for representative microtubule pairs coupled via soft or stiff simulated spring-couplers. Plus-end position data in the top graphs is recopied from Figure 3a. Black traces in the bottom graphs show total force on the two microtubules (F_{TOT}) and demonstrate that a constant total force of F_{TOT} = 8 pN was maintained by the feedback-control. (**b**) Two additional examples of dual-trap assay recordings, formatted as in (a).

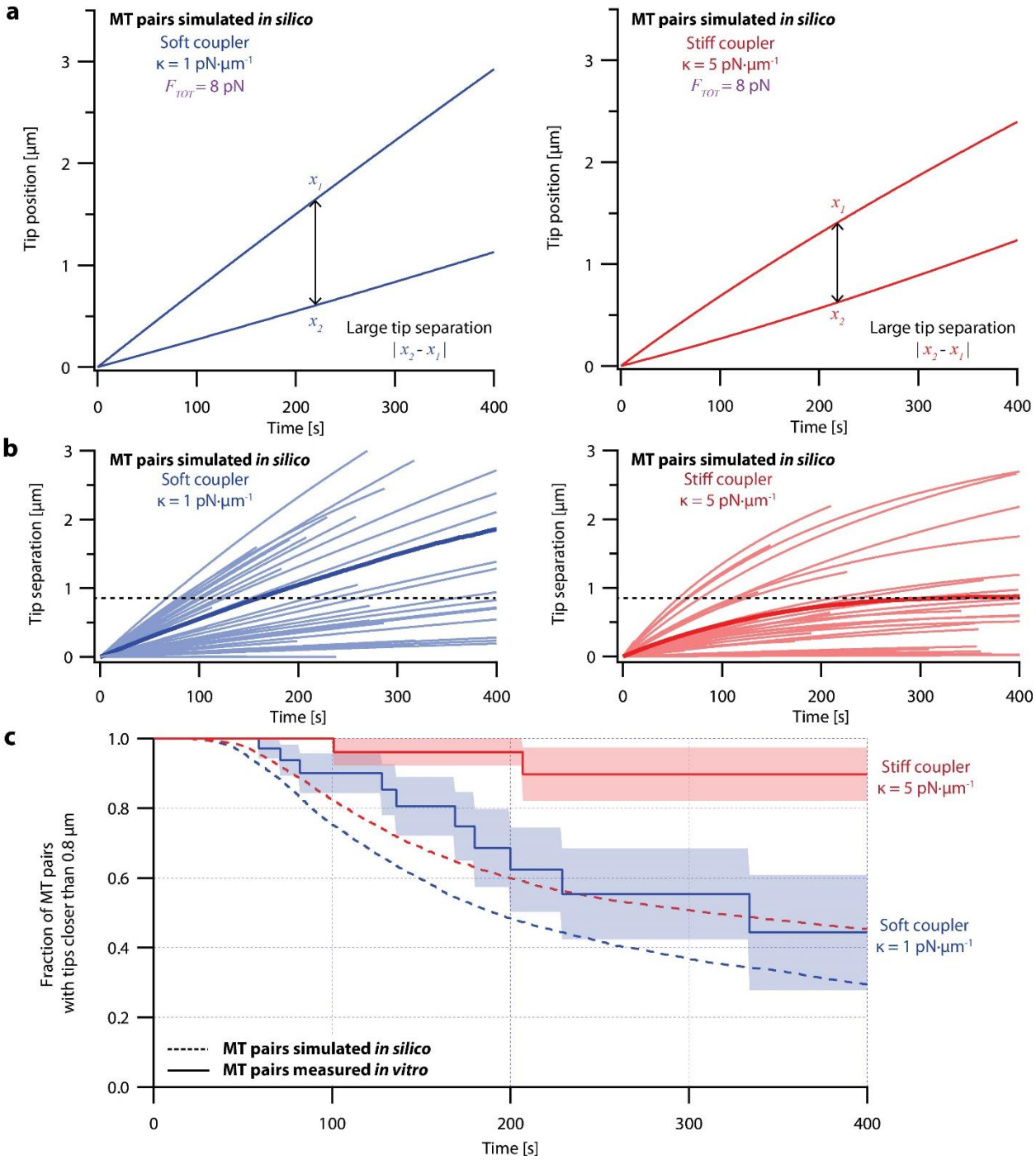

Figure 4. Simple non-pausing simulations fail to recapitulate the coordinated growth of mechanically coupled microtubule pairs. (**a**) Example simulations of microtubule (MT) plus-end positions over time using the non-pausing model. Simulated microtubule pairs were coupled via soft or stiff spring-couplers and shared a total load F_{TOT} = 8 pN to match dual-trap assay conditions. (**b**) Tip separations between microtubule plus-end pairs that were simulated using the non-pausing model and coupled with either soft (left) or stiff (right) spring-couplers. Light colors show tip separations for N = 40 individual simulated microtubule pairs, while dark colors show mean tip separation for N = 10,000 simulated pairs. (**c**) Comparison between the fraction of *in silico* (simulated, dashed curves) and *in vitro* (real, solid curves) microtubule pairs whose plus-ends remained within 0.8 μm of each other over time. Shaded regions show SEMs from N = 50 and N = 43 *in vitro* recordings with soft and stiff couplers, respectively. Soft- and stiff-coupled microtubule pairs were each simulated N = 10,000 times over 400 s of growth in both (b) and (c). Simulation parameters for (a), (b), and (c) can be found in Table 1.

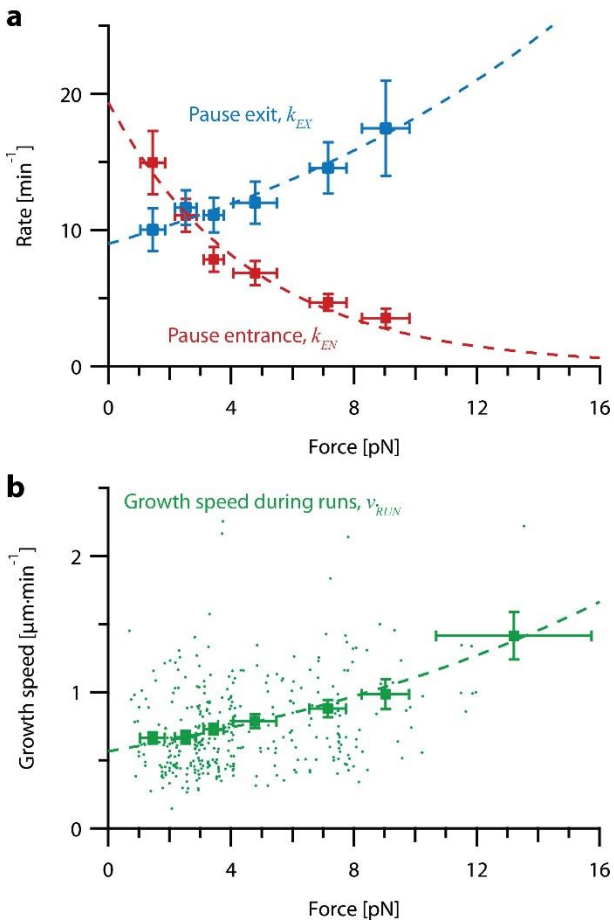

Figure 5. Increasing tension on individual growing microtubules suppresses pausing and accelerates growth during runs. (**a**) As tension on a growing microtubule tip increases, the rate of pause entrance decreases, while the rate of pause exit increases. Mean pause entrance (■) and exit (■) rates (k_{EN} and k_{EX}) were estimated as described in Figure S5-1 and are plotted as functions of force. Error bars show counting uncertainties from N = 25 to 85 individual microtubule recordings and dashed curves show least squares exponential fits. (**b**) As tension on a microtubule tip increases, the growth during runs (i.e., in-between pauses) is accelerated. Points show run speeds measured from recordings of individual microtubules subject to constant tensile forces (from (Akiyoshi et al., 2010)). Symbols (■) represent mean run speeds (v_{RUN}) grouped according to the applied tensile force. Error bars show SEMs from N = 9 to 85 individual microtubule recordings and dashed curve shows the least squares exponential fit. See Figure S5-1 and Materials and Methods for details and Table 1 for fit parameters.

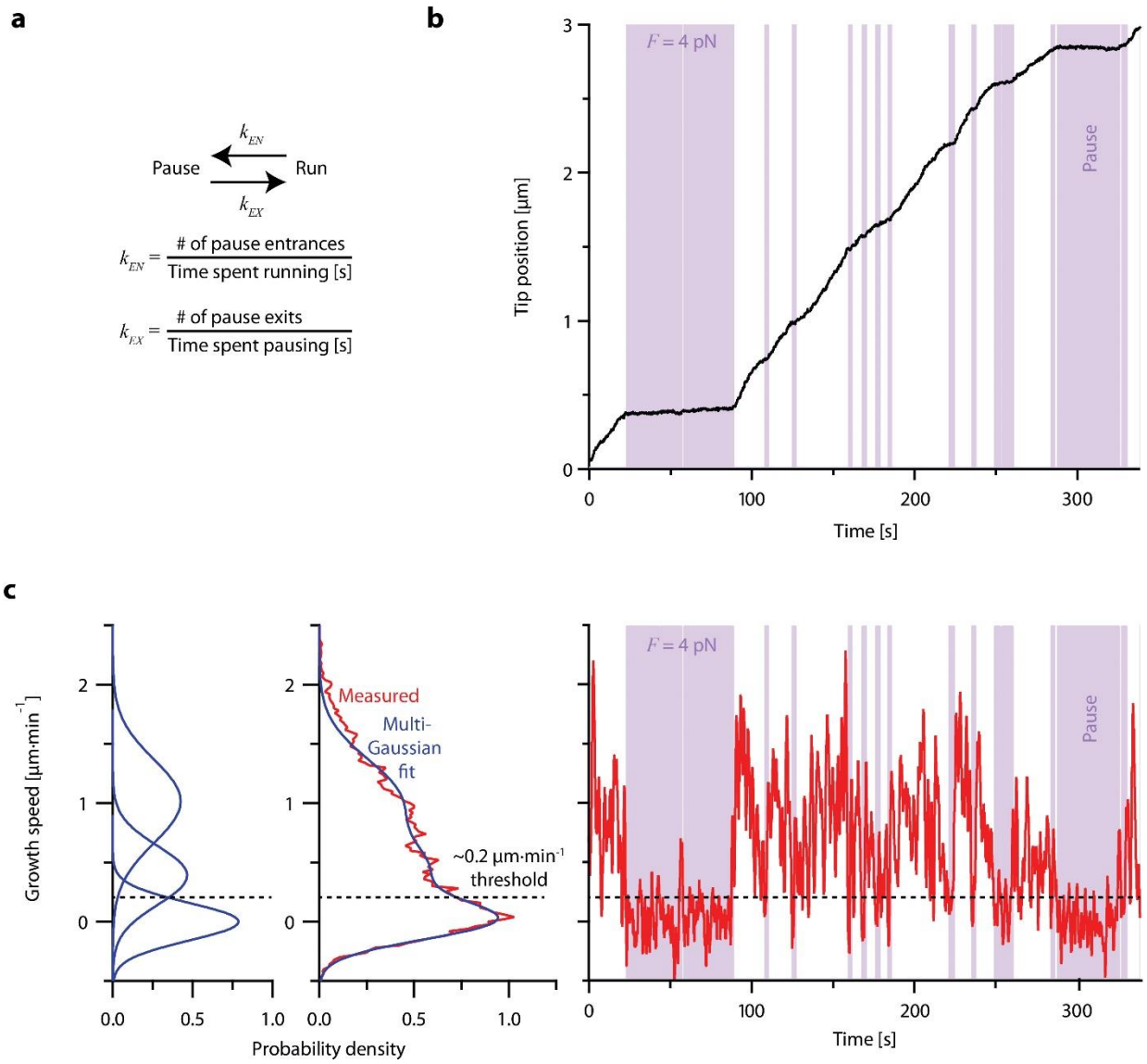

Figure S5-1. Individual microtubules frequently pause during periods of overall growth. (**a**) Growing microtubules switch between states of 'pause,' when plus-end growth speed is nearly zero, and 'run,' when the plus-end is clearly growing. Pause entrance and exit rates, k_{EN} and k_{EX}, were quantified by counting the numbers of entrances or exits and dividing by the total amount of time spent in the run or pause states, respectively. (**b**) Example recording showing plus-end position versus time for an individual microtubule subject to a constant tensile force of 4 pN and exhibiting frequent pauses (denoted by purple shaded regions). This example recording is one of N = 356 force-clamp traces (from (Akiyoshi et al., 2010)) used to estimate the pause entrance and exit rates and growth speeds during runs as functions of force (as shown in Figure 5). (**c**) Classification of runs and pauses. Instantaneous growth speed was computed as a function of time (and plotted at right) from the recording shown in (b), using a 2 s sliding window, and then assembled into a histogram (middle plot, red) and fit with a sum of multiple Gaussian curves (middle and left plots, blue). One Gaussian was always centered at 0 µm·min^{-1} and defined as the 'pause' peak. The intersection of the pause peak and the Gaussian having the next highest mean growth speed was identified for each individual recording and used as a threshold (dashed horizontal line) to distinguish pauses and runs for that recording. Pauses were defined as periods longer than 1 s when the instantaneous growth speed fell below the threshold, while runs were defined as periods longer than 1 s when growth speed was above the threshold (see Materials and Methods for details).

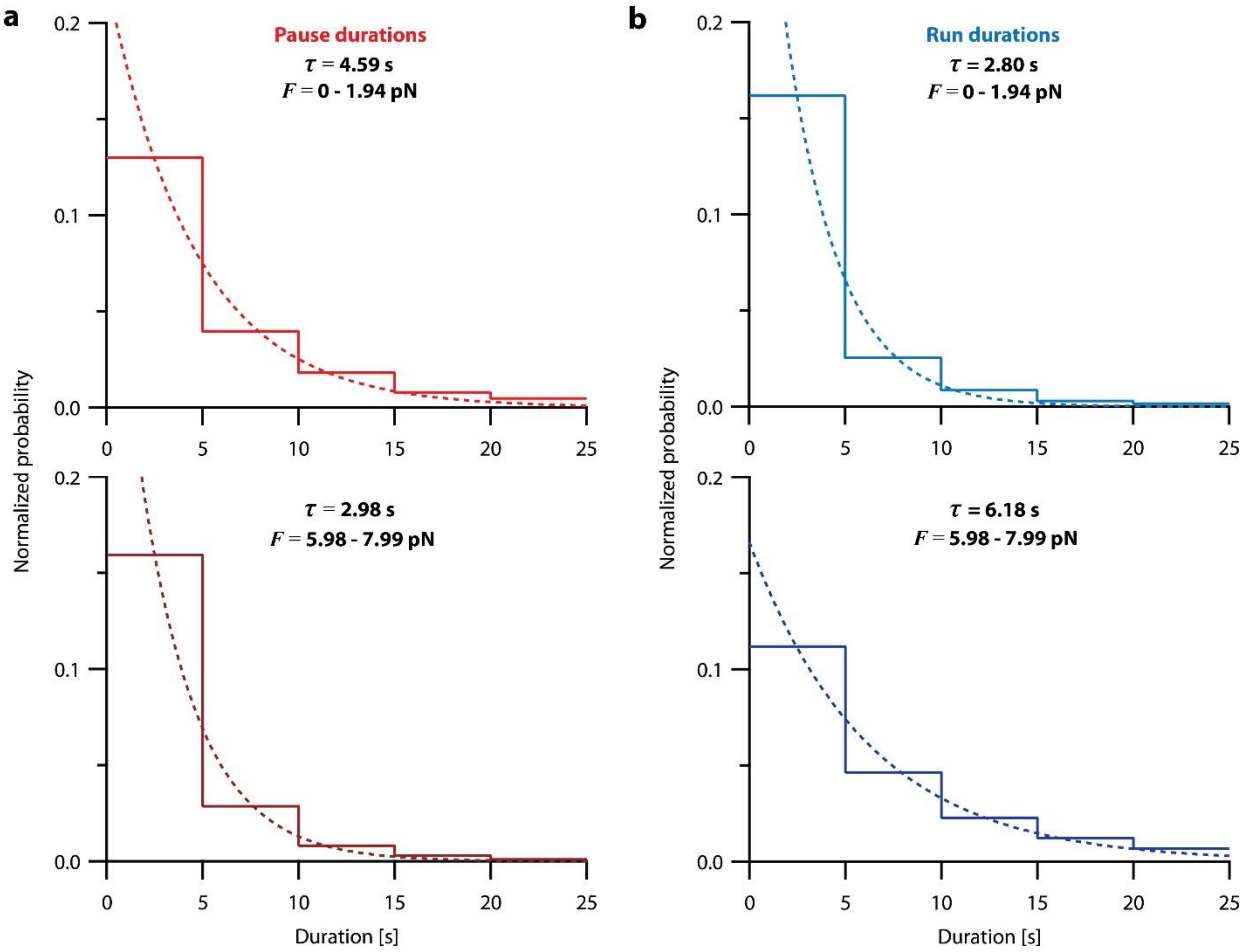

Figure S5-2. Pause and run durations are exponentially distributed. (**a**) Normalized histograms showing pause durations measured from recordings of individual microtubules growing under constant levels of tension (force-clamp data from (Akiyoshi et al., 2010)), either between 0 and 2 pN (top), or between 6 and 8 pN (bottom), corresponding to the lowest and third-highest force bins in Table 2, respectively. (**b**) Normalized histograms showing run durations measured from recordings of individual microtubules growing under constant levels of tension (force-clamp data from (Akiyoshi et al., 2010)), as in (a). For both (a) and (b), least-squares regressions are shown as dashed curves. The indicated time constants (τ) were derived from these fits.

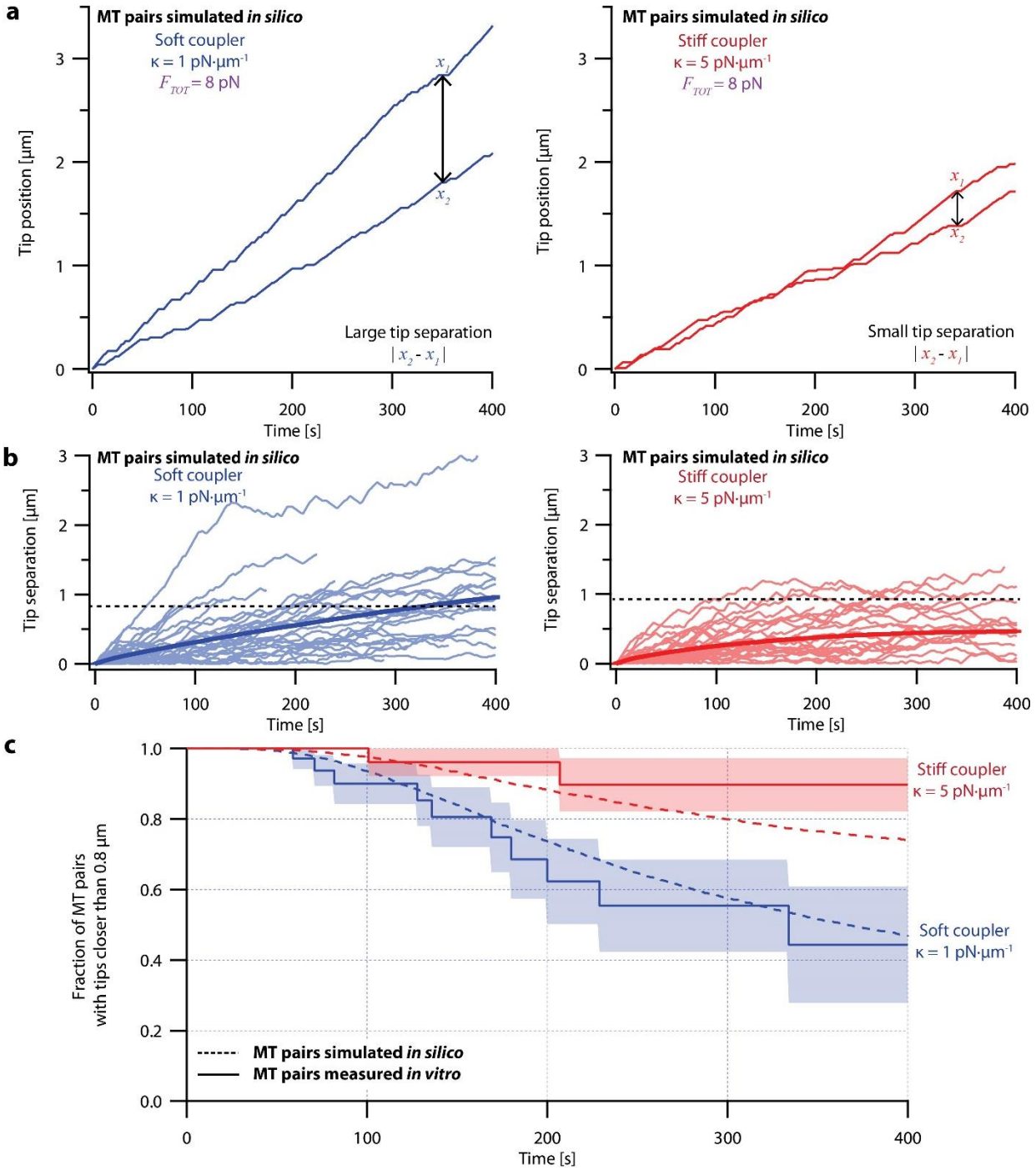

Figure 6. Simulations recapitulate the coordinated growth of mechanically coupled microtubule pairs. (**a**) Example simulations of microtubule (MT) plus-end positions over time using the pausing model. Simulated microtubule pairs were coupled via soft or stiff spring-couplers and shared a total load F_{TOT} = 8 pN to match dual-trap assay conditions. (**b**) Tip separations between microtubule plus-end pairs that were simulated using the pausing model and coupled with either soft (left) or stiff (right) spring-couplers. Light colors show tip separations for N = 40 individual simulated microtubule pairs, while dark curves show mean tip separation for N = 10,000 simulated pairs. (**c**) Comparison between the fraction of *in silico* (simulated, dashed curves) and *in vitro* (real, solid curves) microtubule pairs whose plus-ends remained within 0.8 μm of each other over time. Shaded regions show SEMs from N = 50 and N = 43 *in vitro* recordings with soft and stiff couplers, respectively. Soft- and stiff-coupled microtubule pairs were each simulated N = 10,000 times over 400 s of growth in both (b) and (c). Simulation parameters for (a), (b), and (c) are listed in Table 1.

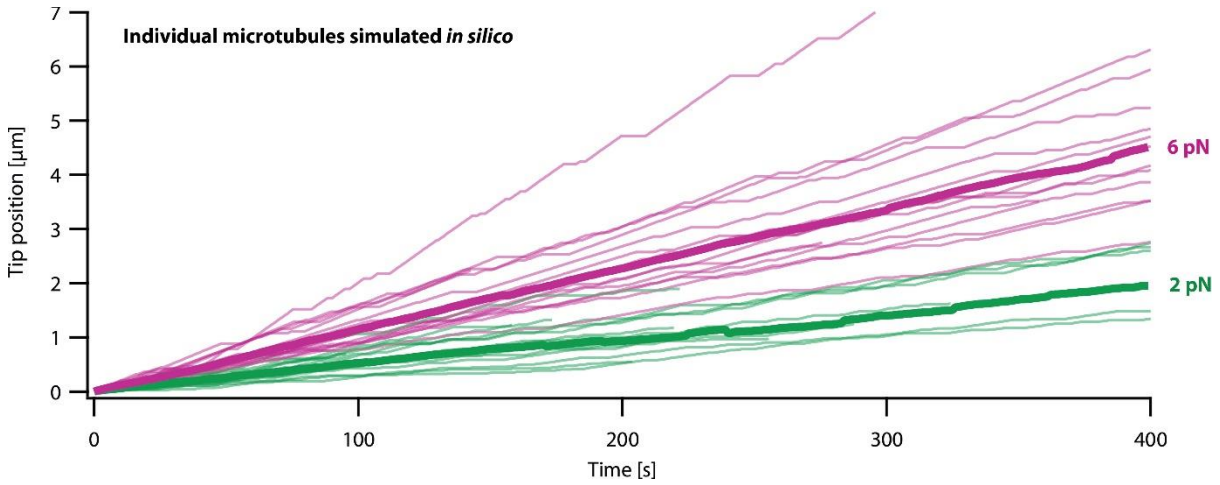

Figure S6-1. Simulations of microtubule growth under constant force using the pausing model resemble real microtubule recordings. Examples using the pausing model to simulate plus-end position versus time for individual growing microtubules subject to a constant tensile force of either 2 or 6 pN (light green or magenta traces, respectively). At each force, N = 16 example simulations are shown, together with the corresponding mean positions versus time (thick traces, computed from the N = 16 individual simulations).

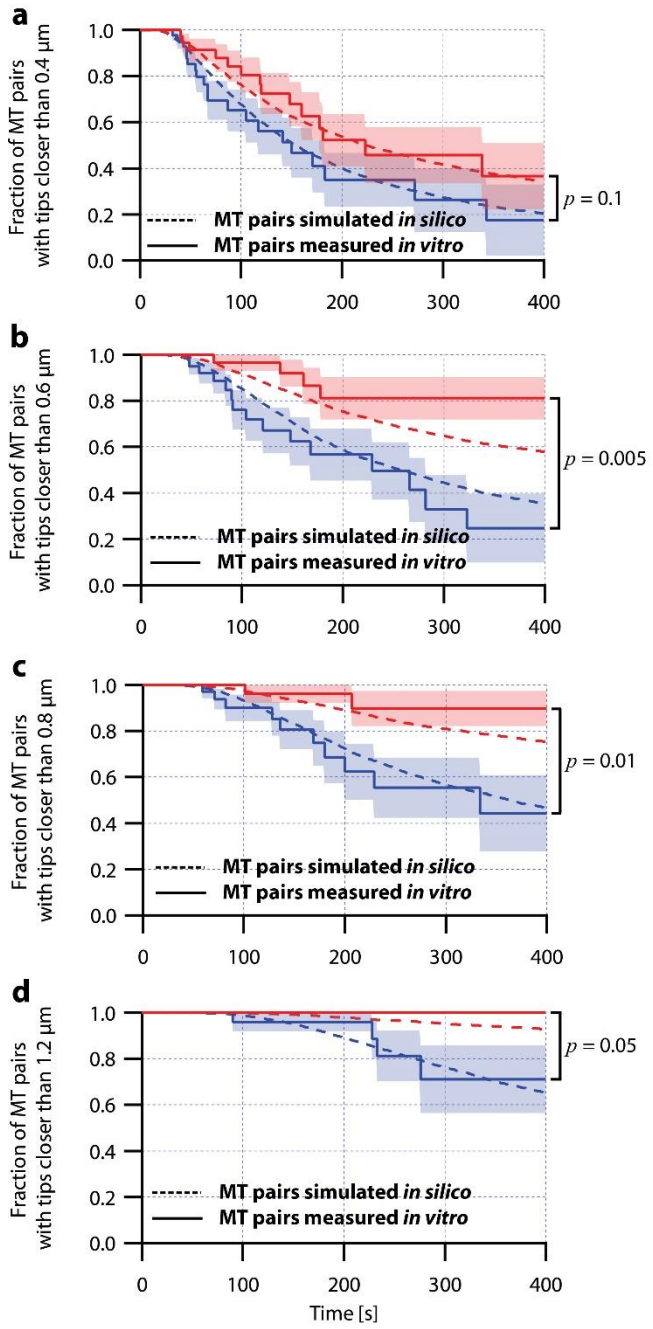

Figure S6-2. Simulations of microtubule pairs using the pausing model maintain tip separations similar to real microtubule pairs. Comparison between the fraction of *in silico* (simulated, dashed curves) and *in vitro* (real, solid curves) microtubule (MT) pairs whose plus-ends remained within (**a**) 0.4 µm, (**b**) 0.6 µm, (**c**) 0.8 µm, and (**d**) 1.2 µm of each other over time. Microtubule pairs *in silico* and *in vitro* shared a total load of F_{TOT} = 8 pN and were coupled via soft or stiff spring couplers. Shaded regions show SEM from N = 50 and N = 43 *in vitro* recordings with soft and stiff couplers, respectively. Soft- and stiff-coupled microtubule pairs were each simulated N = 10,000 times over 400 s of growth. Simulation parameters can be found in Table 1. P-values indicate comparisons between soft- and stiff-coupled microtubule pairs *in vitro* using a log-rank test.

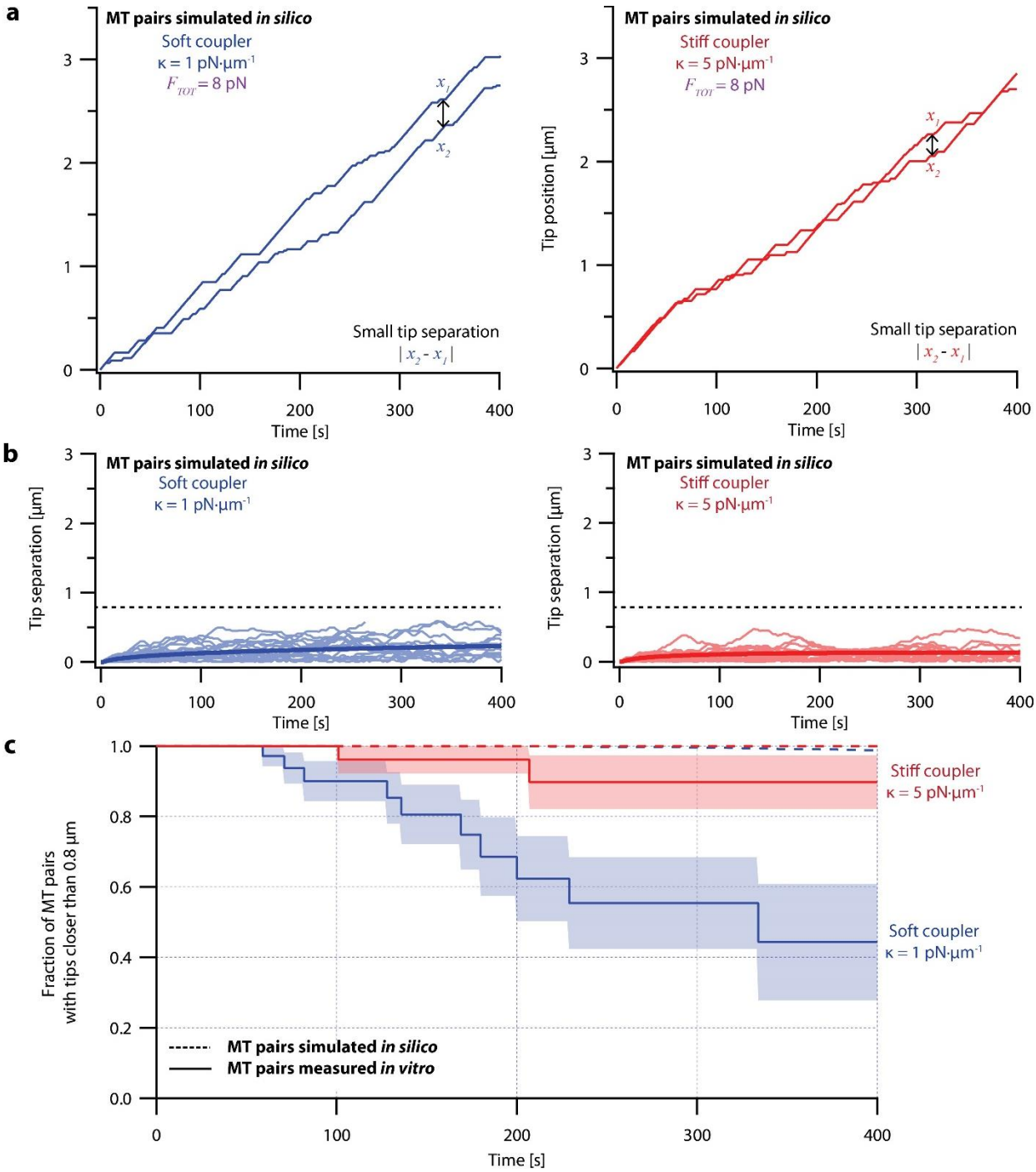

Figure S6-3. Simulations using an ergodic version of the pausing model, without intrinsic heterogeneity, fail to recapitulate the coordinated growth of mechanically coupled microtubules pairs. (**a**) Example simulations of microtubule (MT) plus-end positions over time using the ergodic pausing model. Simulated microtubule pairs were coupled via soft or stiff spring-couplers and shared a total load F_{TOT} = 8 pN to match dual-trap assay conditions. (**b**) Tip separations between microtubule plus-end pairs that were simulated using the ergodic pausing model and coupled with either soft (left) or stiff (right) spring-couplers. Light colors show tip separations for N = 40 individual simulated microtubule pairs while dark colors show mean tip separation for N = 10,000 simulated pairs. (**c**) Comparison between the fraction of *in silico* (simulated, dashed curves) and *in vitro* (real, solid curves) microtubule pairs whose plus-ends remained within 0.8 μm of each other over time. Shaded regions show SEMs from N = 50 and N = 43 *in vitro* recordings with soft and stiff couplers, respectively. Soft- and stiff-coupled microtubule pairs were each simulated N = 10,000 times over 400 s of growth in both (b) and (c). Simulation parameters for (a), (b), and (c) can be

found in Table 1. As expected, microtubule pairs simulated using this ergodic model remained much closer together than real microtubule pairs, rarely separating by more than 0.5 µm irrespective of coupler stiffness. After 300 s, the average tip separation for soft-coupled pairs was only 0.202 ± 0.002 µm (mean ± SEM from N = 10,000 simulations), barely different from the average tip separation for stiff-coupled pairs of 0.134 ± 0.002 µm (mean ± SEM from N = 10,000 simulations). Combined with the success of the non-ergodic pausing model in fitting our dual-trap data, this supports the idea that microtubule growth can be considered non-ergodic during our 400 s experiments.

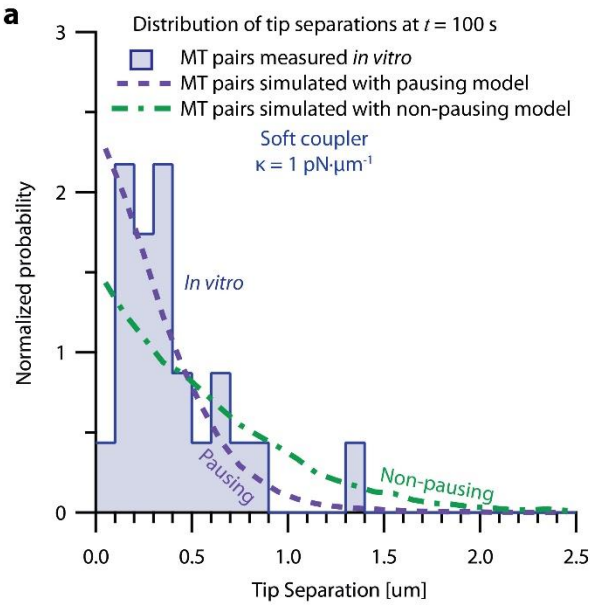

	Mean [μm]	SD [μm]	SEM [μm]	N	Log Likelihood
In vitro	0.39	0.29	0.06	23	N/A
Pausing	0.32	0.27	0.00086	100,397	-15.6
Non-pausing	x	x	x	100,000 +	-16.3

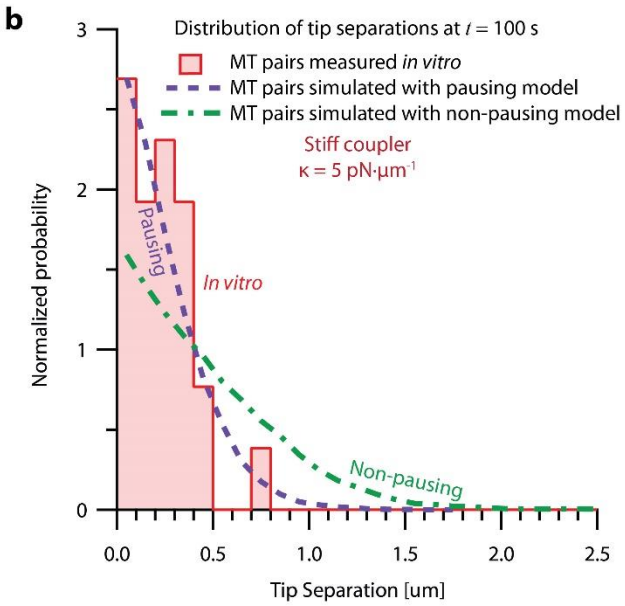

	Mean [μm]	SD [μm]	SEM [μm]	N	Log Likelihood
In vitro	0.23	0.17	0.03	26	N/A
Pausing	0.25	0.21	0.00066	100,000	-10.2
Non-pausing	x	x	x	100,000 +	-13.4

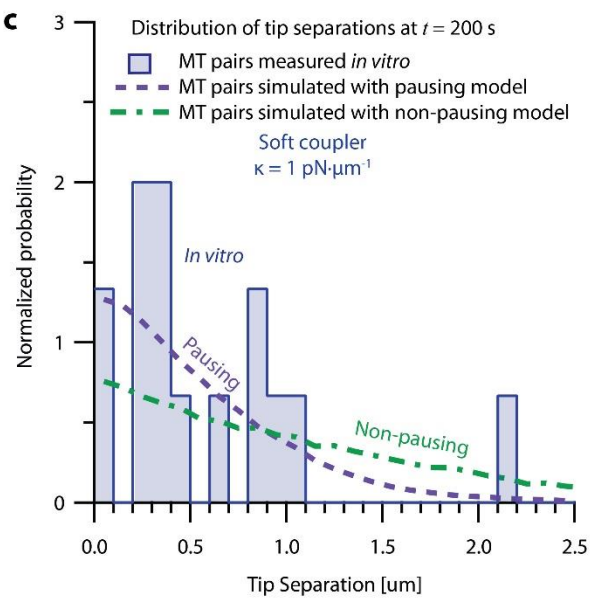

	Mean [μm]	SD [μm]	SEM [μm]	N	Log Likelihood
In vitro	0.60	0.54	0.17	15	N/A
Pausing	0.56	0.48	0.0015	100,000	-18.0
Non-pausing	1.05	0.91	0.0028	104,792	-19.2

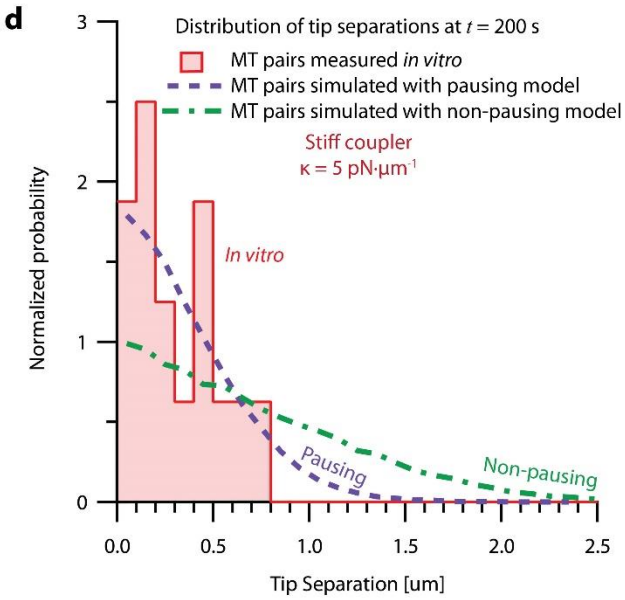

	Mean [μm]	SD [μm]	SEM [μm]	N	Log Likelihood
In vitro	0.31	0.23	0.06	16	N/A
Pausing	0.37	0.29	0.00092	100,000	-14.5
Non-pausing	0.71	0.55	0.0017	100,000	-17.3

Figure S6-4. Probability analysis shows pausing model fits dual-trap recordings better than the non-pausing model. (**Top of each panel**) Histograms of tip separation between microtubule pairs measured in the dual-trap assay and simulated using the pausing and non-pausing model. Soft-coupled pairs are shown on the left ((**a**) and (**c**)), while stiff-coupled pairs are shown on the right ((**b**) and (**d**)). Histograms of tip separations measured 100 s after the start of the recording or simulation are shown on the top ((**a**) and (**b**)), while tip separations measured 200 s after the start of the recording or simulation are shown on the bottom ((**c**) and (**d**)). Tip separation histograms produced by the pausing (purple) and non-pausing model (green) are represented with dashed lines, while dual-trap data is represented by bars. (**Bottom of each panel**) Tables comparing the means, standard deviations (SD), standard errors of the mean (SEM) and numbers of recordings (N) for *in vitro* microtubule pairs and microtubule pairs simulated using the pausing and non-pausing models. The log likelihood probability for each model given the *in vitro* data is shown in the righthand column. The greater the log likelihood, the greater the probability that the given model could reproduce the measured *in vitro* data. At both 100 s and 200s, for soft and stiff couplers, the pausing model scores higher than the non-pausing model, indicating that the pausing model is a better fit to our *in vitro* data.

Parameter name	Parameter symbol	Relevant equation	Parameter estimate	Applicable models	Reference
Growth speed force sensitivity	F_g	$v_g = v_{g0}\exp(F/F_g)$	8.4 pN	non-pausing	Akiyoshi et al., 2010 Figure 4e
Unloaded pause entrance rate	k_{EN0}	$k_{EN} = k_{EN0}\exp(F/F_{EN})$	19.4 min^{-1}	pausing	Figure 5a, red
Pause entrance rate force sensitivity	F_{EN}	$k_{EN} = k_{EN0}\exp(F/F_{EN})$	-4.6 pN	pausing	Figure 5a, red
Unloaded pause exit rate	k_{EX0}	$k_{EX} = k_{EX0}\exp(F/F_{EX})$	9.0 min^{-1}	pausing	Figure 5a, blue
Pause exit rate force sensitivity	F_{EX}	$k_{EX} = k_{EX0}\exp(F/F_{EX})$	14.1 pN	pausing	Figure 5a, blue
Unloaded run speed	v_0	$v_{RUN} = v_0\exp(F/F_{RUN})$	0.52 $\mu m \cdot min^{-1}$	neither	Figure 5b
Run speed force sensitivity	F_{RUN}	$v_{RUN} = v_0\exp(F/F_{RUN})$	14.8 pN	pausing	Figure 5b

Table 1. Parameter table for coupled microtubule pairs simulated for non-pausing and pausing models. Relevant parameters measured from constant force recordings from (Akiyoshi et al., 2010). These parameters were used to simulate coupled microtubule pairs using each of the models described in the main text. The equation in which each parameter is used, as well as which models of microtubule growth use that equation, are indicated.

Bin number	N	Lower bound [pN]	Upper bound [pN]	Pause entrances	Time in pause [s]	Pause exits	Time in run [s]
1	41	0.69	1.94	1834	10957	1830	7364
2	85	1.94	2.97	3502	18047	3501	18952
3	77	2.97	3.999	2376	12842	2374	18159
4	60	3.999	5.98	1937	9661	1932	16993
5	60	5.98	7.99	1439	5930	1438	18465
6	25	7.99	10.3	387	1298	378	6559
7	9	10.3	18	23	93	23	712

Table 2. Number of recordings, bounds, and pause quantification from force-clamp dataset, binned by force. Table describing constant force recordings in (Akiyoshi et al., 2010) and the pause quantification performed in the current work. N indicates the number of recordings in a particular bin. For consistency, these force bins are identical to those used in (Akiyoshi et al., 2010).

References

Akiyoshi, B., Sarangapani, K. K., Powers, A. F., Nelson, C. R., Reichow, S. L., Arellano-Santoyo, H., Gonen, T., Ranish, J. A., Asbury, C. L., & Biggins, S. (2010). Tension directly stabilizes reconstituted kinetochore-microtubule attachments. *Nature*, *468*(7323), 576-579. https://doi.org/10.1038/nature09594

Al-Bassam, J., Kim, H., Brouhard, G., van Oijen, A., Harrison, S. C., & Chang, F. (2010). CLASP promotes microtubule rescue by recruiting tubulin dimers to the microtubule. *Dev Cell*, *19*(2), 245-258. https://doi.org/10.1016/j.devcel.2010.07.016

Amaro, A. C., Samora, C. P., Holtackers, R., Wang, E., Kingston, I. J., Alonso, M., Lampson, M., McAinsh, A. D., & Meraldi, P. (2010). Molecular control of kinetochore-microtubule dynamics and chromosome oscillations. *Nature Cell Bio*, *12*(4), 319-329. https://doi.org/10.1038/ncb2033

Amin, M. A., Agarwal, S., & Varma, D. (2019). Mapping the kinetochore MAP functions required for stabilizing microtubule attachments to chromosomes during metaphase. *Cytoskeleton*, *76*(6), 398-412. https://doi.org/10.1002%2Fcm.21559

Amoah-Darko, F. L., & White, D. (2022). Modelling microtubule dynamic instability: Microtubule growth, shortening and pause. *J Theor Biol*, *553*, 111257-111257. https://doi.org/10.1016/j.jtbi.2022.111257

Asbury, C. L., Gestaut, D. R., Powers, A. F., Franck, A. D., & Davis, T. N. (2006). The Dam1 kinetochore complex harnesses microtubule dynamics to produce force and movement. *Proc Natl Acad Sci U S A*, *103*(26), 9873-9878. https://doi.org/10.1073/pnas.0602249103

Bakhoum, S. F., & Compton, D. A. (2012). Kinetochores and disease: keeping microtubule dynamics *in check! Curr Opinion in Cell Biol*, *24*(1), 64-70. https://doi.org/10.1016/j.ceb.2011.11.012

Bakhoum, S. F., Genovese, G., & Compton, D. A. (2009). Deviant kinetochore microtubule dynamics underlie chromosome instability. *Curr Biol*, *19*(22), 1937-1942. https://doi.org/10.1016/j.cub.2009.09.055

Banigan, E., Chiou, K., Ballister, E. R., Mayo, A. M., Lampson, M. A., & Liu, A. J. (2015). Minimal model for collective kinetochore-microtubule dynamics. *PNAS*, *112*(41), 12699-12704. https://doi.org/10.1073/pnas.1513512112

Brouhard, G., & Rice, L. M. (2018). Microtubule Dynamics: an interplay of biochemistry and mechanics. *Nat Rev Mol Cell Biol*, *19*(7), 451-463. https://doi.org/10.1038/s41580-018-0009-y

Brouhard, G. J. (2015). Dynamic instability 30 years later: complexities in microtubule growth and catastrophe. *MBoC*, *26*(7), 1207-1210. https://doi.org/10.1091/mbc.E13-10-0594

Brouhard, G. J., Stear, J. H., Noetzel, T. L., Al-Bassam, J., Kinoshita, K., Harrison, S. C., Howard, J., & Hyman, A. A. (2008). XMAP215 is a processive microtubule polymerase. *Cell*, *132*(1), 79-88. https://doi.org/10.1016/j.cell.2007.11.043

Cassimeris, L., Pryer, N. K., & Salmon, E. D. (1988). Real-time observations of microtubule dynamic instability in living cells. *J Cell Biol*, *107*(6), 2223-2231. https://doi.org/10.1083/jcb.107.6.2223

Castrogiovanni, C., Inchingolo, A. V., Harrison, J. U., Dudka, D., Sen, O., Burroughs, N. J., McAinsh, A. D., & Meraldi, P. (2021). Evidence for a HURP/EB free mixed nucleotide zone in kinetochore-microtubules. *Nature communications*, *13*(1). https://doi.org/10.1038/s41467-022-32421-x

Chacon, J. M., Mukherjee, S., Schuster, B. M., Clarke, D. J., & Gardner, M. K. (2014). Pericentromere tension is self-regulated by spindle structure in metaphase. *J Cell Biol*, *205*(3), 313-324. https://doi.org/10.1083/jcb.201312024

Cheung, Y. K., & Klotz, J. H. (1997). The Mann Whitney Wilcoxon distribution using linked lists. *Statistica Sinica*, *7*, 805-813. https://www3.stat.sinica.edu.tw/statistica/oldpdf/a7n316.pdf

Chretien, D., Metoz, F., Verde, F., Karsenti, E., & Wade, R. H. (1992). Lattice defects in microtubules: protofilament numbers vary within individual microtubules. *J Cell Biol*, *117*(5), 1031-1040. https://doi.org/10.1083/jcb.117.5.1031

Cimini, D., Cameron, L. A., & Salmon, E. D. (2004). Anaphase spindle mechanics prevent mis-segregation of merotelically oriented chromosomes. *Curr Biol*, *14*(23), 2149-2155. https://doi.org/10.1016/j.cub.2004.11.029

Cleary, J. M., & Hancock, W. O. (2021). Molecular mechanisms underlying microtubule growth dynamics. *Curr Biol*, *31*(10), R560-R573. https://doi.org/10.1016/j.cub.2021.02.035

Cleary, J. M., Kim, T., Cook, A. S. I., McCormick, L. A., Hancock, W. O., & Rice, L. M. (2022). Measurements and simulations of microtubule growth imply stron longitudinal interactions and reveal a role for GDP on the elongating end. *Elife*, *11*. https://doi.org/10.7554/eLife.75931

Cojoc, G., Roscioli, E., Zhang, L., Garcia-Ulloa, A., Shah, J. V., Berns, M. W., Pavin, N., Cimini, D., Tolic, I. M., & Gregan, J. (2016). Laser microsurgery reveals conserved viscoelastic behavior of the kinetochore. *J Cell Biol*, *212*(7), 767-776. https://doi.org/10.1083/jcb.201506011

Coombes, C. E., Yamamoto, A., Kenzie, M. R., Odde, D. J., & Gardner, M. K. (2013). Evolving tip structures can explain age-dependent microtubule catastrophe. *Curr Biol*, *23*(14), 1342-1348. https://doi.org/10.1016/j.cub.2013.05.059

Das, D., Das, D., & Padinhateeri, R. (2014). Force-induced dynamical properties of multiple cytoskeletal filaments are distinct from that of single filaments. *PLoS one*, *9*(12). https://doi.org/10.1371/journal.pone.0114014

Dogterom, M., & Yurke, B. (1997). Measurement of the force-velocity relation for growing microtubules [In Vitro]. *Science*, *278*(5339), 856-860. http://www.ncbi.nlm.nih.gov/pubmed/9346483

Driver, J. W., Geyer, E. A., Bailey, M. E., Rice, L. M., & Asbury, C. L. (2017). Direct measurement of conformational strain energy in protofilaments curling outward from disassembling microtubule tips. *Elife*, *6*. https://doi.org/10.7554/eLife.28433

Ertych, N., Stolz, A., Stenzinger, A., Weichert, W., KaulfuB, S., Burfeind, P., Aigner, A., Wordeman, L., & Bastians, H. (2014). Increased microtubule assembly rates influence chromosomal instability in colorectal cancer cells. *Nature Cell Bio*, *16*(8), 779-791. https://doi.org/10.1038/ncb2994

Franck, A. D., Powers, A. F., Gestaut, D. R., Davis, T. N., & Asbury, C. L. (2010). Direct physical study of kinetochore-microtubule interactions by reconstitution and interrogation with an optical force clamp [Review]. *Methods*, *51*(2), 242-250. https://doi.org/10.1016/j.ymeth.2010.01.020

Gardner, M. K., & Odde, D. J. (2010). Stochastic simulation and graphic visualization of mitotic processes. *Methods*, *51*(2), 251-256. https://doi.org/10.1016/j.ymeth.2010.01.021

Gardner, M. K., Pearson, C. G., Sprague, B. L., Zarzar, T. R., Bloom, K., Salmon, E. D., & Odde, D. J. (2005). Tension-dependent regulation of microtubule dynamics at kinetochores can explain metaphase congression in yeast. *Mol Biol Cell*, *16*(8), 3764-3775. https://doi.org/10.1091/mbc.E05-04-0275

Garner, R. M., & Theriot, J. A. (2022). Leading edge maintenance in migrating cells is an emergent property of branched actin network growth. *Elife*, *11*. https://doi.org/10.7554/eLife.74389

Gaudenz, D., Matov, A., Wittman, T., Kumar, P., Thoma, C., Applegate, K., & Krek, W. (2010). Analysis of microtubule dynamic instability using a plus-end growth marker. *Nature methods*, *7*(9), 761-768. https://doi.org/10.1038/NMETH.1493

Geisterfer, Z. M., Zhu, D. Y., Mitchison, T. J., Oakey, J., & Gatlin, J. C. (2020). Microtubule growth rates are sensitive to global and local changes in microtubule plus-end density. *Curr Biol*, *30*(15), 3016-3023. https://doi.org/10.1016/j.cub.2020.05.056

Ghanti, D., & Chowdhury, D. (2015). Collective cargo hauling by a bundle of parallel microtubules: bi-directional motion caused by load-dependent polymerization and depolymerization. *J Stat Mech*, *2015*(1), 1008-1013. https://doi.org/10.1088/1742-5468/2015/01/P01008

Gildersleeve, R. F., Cross, A. R., Cullen, K. E., Fagen, A. P., & Williams, R. C. J. (1992). Microtubules grow and shorten at intrinsically variable rates. *J Biol Chem*, *267*(12), 7995-8006. https://www.jbc.org/article/S0021-9258(18)42399-X/pdf

Goshima, G., Wollman, R., Stuurman, N., Scholey, J. M., & Vale, R. D. (2005). Length control of the metaphase spindle. *Curr Biol*, *15*(22), 1979-1988. https://doi.org/10.1016/j.cub.2005.09.054

Holzbaur, E. L. F., & Goldman, Y. E. (2010). Coordination of molecular motors: from *in vitro* assays to intracellular dynamics. *Curr Opinion in Cell Biol*, *22*(1), 4-13. https://doi.org/10.1016/j.ceb.2009.12.014

Howard, J. (2001). *Mechanics of motor proteins and the cytoskeleton*. Sinauer Associates, Publishers.

Janson, M. E., de Dood, M. E., & Dogterom, M. (2003). Dynamic instability of microtubules is regulated by force. *J Cell Biol*, *161*(6), 1029-1034. https://doi.org/10.1083/jcb.200301147

Khodjakov, A., Cole, R. W., Bajer, A. S., & Rieder, C. L. (1996). The force for poleward chromosome motion in Haemanthus cells acts along the length of the chromosome during metaphase but only at the kinetochore during anaphase. *J Cell Biol*, *132*(6), 1093-1104. http://www.ncbi.nlm.nih.gov/pubmed/8601587

Khodjakov, A., & Rieder, C. L. (1996). Kinetochores moving away from their associated pole do not exert a significant pushing force on the chromosome. *J Cell Biol*, *135*(2), 315-327. http://www.ncbi.nlm.nih.gov/pubmed/8896591

Kiewisz, R., Fabig, G., Conway, W., Baum, D., Needleman, D., & Muller-Reichert, T. (2022). Three-dimensional structure of kinetochore-fibers in human mitotic spindles. *Elife*, *11*. https://doi.org/10.7554/eLife.75459

Kis, A., Kasas, S., Babic, B., Kulik, A. J., Benoit, W., Briggs, G. A., Schonenberger, C., Catsicas, S., & Forro, L. (2002). Nanomechanics of microtubules. *Phys Rev Lett*, *89*(24), 248101. https://doi.org/10.1103/PhysRevLett.89.248101

Klotz, J. H. (2006). *A Computational Approach to Statistics*. https://www.mimuw.edu.pl/~pokar/StatystykaI/Literatura/KlotzBook.pdf

Laan, L., Husson, J., Munteanu, E. L., Kerssemakers, J. W. J., & Dogterom, M. (2008). Force-generation and dynamic instability of microtubule bundles. *105*(26), 8920-8925. https://doi.org/10.1073/pnas.0710311105

Maddox, P., Straight, A., Coughlin, P., Mitchison, T. J., & Salmon, E. D. (2003). Direct observation of microtubule dynamics at kinetochores in Xenopus extract spindles: implications for spindle mechanics. *J Cell Biol*, *162*(3), 377-382. https://doi.org/10.1083/jcb.200301088

Mahserejian, S. M., Scripture, J. P., Mauro, A. J., Lawrence, E. J., Jonasson, E. M., Murray, K. S., Li, J., Gardner, M., Alber, M., Zanic, M., & Goodson, H. V. (2022). Quantification of microtubule stutters: dynamic instability behaviors that are strongly associated with catastrophe. *MBoC*, *33*(3). https://doi.org/10.1091/mbc.E20-06-0348

Maiato, H., Fairley, E. A. L., Rieder, C. L., Swedlow, J. R., Sunkel, C. E., & Earnshaw, W. C. (2003). Human CLASP1 is an outer kinetochore component that regulates spindle microtubule dynamics. *Cell*, *113*(7), 891-904. https://doi.org/10.1016/S0092-8674(03)00465-3

Maiato, H., Rieder, C. L., Earnshaw, W. C., & Sunkel, C. E. (2003). How do kinetochores CLASP dynamic microtubules? *Cell Cycle*, *2*(6), 511-514. https://doi.org/10.4161/cc.2.6.576

McAinsh, A. D., & Meraldi, P. (2011). The CCAN complex: Linking centromere specification to control of kinetochore-microtubule dynamics. *Seminars in Cell & Dev Biol*, *22*(9), 946-952. https://doi.org/10.1016/j.semcdb.2011.09.016

McDonald, K. L., O'Toole, E. T., Mastronarde, D. N., & McIntosh, J. R. (1992). Kinetochore microtubules in PTK cells. *J Cell Biol*, *118*(2), 369-383. http://www.ncbi.nlm.nih.gov/pubmed/1629239

McIntosh, J. R., O'Toole, E., Morgan, G., Austin, J., Ulyanov, E., Ataullakhanov, F., & Gudimchuk, N. (2018). Microtubules grow by the addition of bent guanosine triphosphate tubulin to the tips of curved protofilaments [Article]. *Journal of Cell Biology*, *217*(8), 2691-2708. https://doi.org/10.1083/jcb.201802138

Miller, M. P., Asbury, C. L., & Biggins, S. (2016). A TOG Protein Confers Tension Sensitivity to Kinetochore-Microtubule Attachments. *Cell*, *165*(6), 1428-1439. https://doi.org/10.1016/j.cell.2016.04.030

Murray, L. E., Kim, H., Rice, L. M., & Asbury, C. L. (2022). Working strokes produced by curling protofilaments at disassembling microtubule tips can be biochemically tuned and vary with species. *Elife*, *11*. https://doi.org/10.7554/eLife.83225

Neahring, L., Cho, N. H., & Dumont, S. (2021). Opposing motors provide mechanical and functional robustness in the human spindle. *Dev Cell*, *56*(21), 3006-3018. https://doi.org/10.1016/j.devcel.2021.09.011

Nicklas, R. B. (1983). Measurements of the force produced by the mitotic spindle in anaphase. *J Cell Biol*, *97*(2), 542-548. http://www.ncbi.nlm.nih.gov/pubmed/6885908

Nicklas, R. B. (1988). The forces that move chromosomes in mitosis. *Annu Rev Biophys Biophys Chem*, *17*, 431-449. https://doi.org/10.1146/annurev.bb.17.060188.002243

O'Toole, E., Morphew, M., & McIntosh, J. R. (2020). Electron tomography reveals aspects of spindle structure important for mechanical stability at metaphase. *Molecular Biology of the Cell*, *31*(3), 184-195. https://doi.org/10.1091/mbc.E19-07-0405

Ou, G., & Scholey, J. M. (2022). Motor cooperation during mitosis and ciliogenesis. *Annu Rev Cell Dev Biol*, *38*(1), 49-74. https://doi.org/10.1146/annurev-cellbio-121420-100107

Pampaloni, F., Lattanzi, G., Jonas, A., Surrey, T., Frey, E., & Florin, E. L. (2006). Thermal fluctuations of grafted microtubules provide evidence of a length-dependent persistence length. *Proc Natl Acad Sci U S A*, *103*(27), 10248-10253. https://doi.org/10.1073/pnas.0603931103

Poirier, M. G., Eroglu, S., & Marko, J. F. (2002). The bending rigidity of mitotic chromosomes. *MBoC*, *13*(6), 2170-2179. https://doi.org/10.1091/mbc.01-08-0401

Powers, A. F., Franck, A. D., Gestaut, D. R., Cooper, J., Gracyzk, B., Wei, R. R., Wordeman, L., Davis, T. N., & Asbury, C. L. (2009). The Ndc80 kinetochore complex forms load-bearing attachments to dynamic microtubule tips via biased diffusion. *Cell*, *136*(5), 865-875. https://doi.org/10.1016/j.cell.2008.12.045

Press, W. H., Flannery, B. P., Teukolsky, S. A., & Vetterling, W. T. *Numerical Recipes in C: The Art of Scientific Computing*.

Rai, A., Liu, T., Katrukha, E. A., Estevez-Gallego, J., Manka, S. W., Paterson, I., Diaz, J. F., Kapitein, L. C., Moores, C. A., & Akhmanova, A. (2021). Lattice defects induced by microtubule-stabilizing agents exert a long-range effect on microtubule growth by promoting catastophes. *PNAS*, *118*(51). https://doi.org/10.1073/pnas.2112261118

Renda, F., Magidson, V., Tikhonenko, I., Fisher, R., Miles, C., Mogilner, A., & Khodjakov, A. (2020). Effects of malleable kinetochore morphology on measurements of intrakinetochore tension. *Open Biol*, *10*(7). https://doi.org/10.1098/rsob.200101

Risteski, P., Jagric, M., Pavin, N., & Tolic, I. M. (2021). Biomechanics of chromosome alignment at the spindle midplane. *Curr Biol*, *31*(10), R574-R585. https://doi.org/10.1016/j.cub.2021.03.082

Rizk, R. S., Bohannon, K. P., Wetzel, L. A., Powers, J., Shaw, S. L., & Walczak, C. E. (2009). MCAK and paclitaxel have differential effects on spindle microtubule organization and dynamics. *MBoC*, *20*(6), 1639-1651. https://doi.org/10.1091/mbc.e08-09-0985

Sanhaji, M., Friel, C. T., Wordeman, L., Louwen, F., & Yuan, J. (2011). Mitotic centromere-associated kinesin (MCAK): a potential cancer drug target. *Oncotarget*, *2*(12), 935-947. https://doi.org/10.18632/oncotarget.416

Sarangapani, K. K., Akiyoshi, B., Duggan, N. M., Biggins, S., & Asbury, C. L. (2013). Phosphoregulation promotes release of kinetochores from dynamic microtubules via multiple mechanisms. *Proc Natl Acad Sci U S A*, *110*(18), 7282-7287. https://doi.org/10.1073/pnas.1220700110

Schwietert, F., & Kierfeld, J. (2020). Bistability and oscillations in cooperative microtubule and kinetochore dynamics in the mitotic spindle. *New journal of physics*, *22*(5). https://doi.org/10.1088/1367-2630/ab7ede

Schwietert, F., Volkov, V. A., Pim J., H. V., Dogterom, M., Musacchio, A., & Kierfeld, J. (2022). Strain stiffening of Ndc80 complexes attached to microtubule plus ends. *Biophys J*, *121*(21), 4048-4062. https://doi.org/10.1016/j.bpj.2022.09.039

Skibbens, R. V., Rieder, C. L., & Salmon, E. D. (1995). Kinetochore motility after severing between sister centromeres using laser microsurgery: evidence that kinetochore directional instability and position is regulated by tension. *J Cell Sci*, *108 (Pt 7)*, 2537-2548. http://www.ncbi.nlm.nih.gov/pubmed/7593295

Skibbens, R. V., Skeen, V. P., & Salmon, E. D. (1993). Directional instability of kinetochore motility during chromosome congression and segregation in mitotic newt lung cells: a push-pull mechanism. *J Cell Biol*, *122*(4), 859-875. http://www.ncbi.nlm.nih.gov/pubmed/8349735

Sousa, A., Reis, R., Sampaio, P., & Sunkel, C. E. (2007). The *Drosophila* CLASP homologue, Mast/Orbit regulates the dynamic behaviour of interphase microtubules by promoting the pause state. *Cell Motility*, *64*(8), 605-620. https://doi.org/10.1002/cm.20208

Streitberg, B., & Rohmel, J. (1986). Exact distributions for permutations and rank tests: An introduction to some recently published algorithms. *Statistical Software Newsletter*, *12*, 10-17.

Stumpff, J., Ghule, P. N., Shimamura, A., Stein, J. L., & Greenblatt, M. (2014). Spindle microtubule dysfunction and cancer predisposition. *J Cell Phys*, *229*(12), 1881-1883. https://onlinelibrary.wiley.com/doi/abs/10.1002/jcp.24691

Stumpff, J., Wagenbach, M., Franck, A., Asbury, C. L., & Wordeman, L. (2012). Kif18A and chromokinesins confine centromere movements via microtubule growth suppression and spatial control of kinetochore tension. *Dev Cell*, *22*(5), 1017-1029. https://doi.org/10.1016/j.devcel.2012.02.013

Tien, J. F., Umbreit, N. T., Gestaut, D. R., Franck, A. D., Cooper, J., Wordeman, L., Gonen, T., Asbury, C. L., & Davis, T. N. (2010). Cooperation of the Dam1 and Ndc80 kinetochore complexes enhances microtubule coupling and is regulated by aurora B. *J Cell Biol*, *189*(4), 713-723. https://doi.org/10.1083/jcb.200910142

Tirnauer, J. S., Canman, J. C., Salmon, E. D., & Mitchison, T. J. (2002). EB1 targets to kinetochores with attached, polymerizing microtubules. *MBoC*, *13*(12), 4308-4316. https://doi.org/10.1091/mbc.E02-04-0236

VandenBeldt, K. J., Barnard, R. M., Hergert, P. J., Meng, X., Maiato, H., & McEwen, B. F. (2006). Kinetochores use a novel mechanism for coordinating the dynamics of individual microtubules. *Curr Biol*, *16*(12), 1217-1223. https://doi.org/10.1016/j.cub.2006.04.046

Varga, V., Helenius, J., Tanaka, K., Hyman, A. A., Tanaka, T. U., & Howard, J. (2006). Yeast kinesin-8 depolymerizes microtubules in a length-dependent manner. *Nat Cell Biol*, *8*(9), 957-962. http.://doi.org/10.1038/ncb1462

Volkov, V. A., Huis In 't Veld, P. J., Dogterom, M., & Musacchio, A. (2018). Multivalency of NDC80 in the outer kinetochore is essential to track shortening microtubules and generate forces. *Elife*, *7*. https://doi.org/10.7554/eLife.36764

Wan, X., Cimini, D., Cameron, L. A., & Salmon, E. D. (2012). The coupling between sister kinetochore directional instability and oscillations in centromere stretch in metaphase PtK1 cells. *Mol Biol Cell*, *23*(6), 1035-1046. https://doi.org/10.1091/mbc.E11-09-0767

Waters, J. C., Skibbens, R. V., & Salmon, E. D. (1996). Oscillating mitotic newt lung cell kinetochores are, on average, under tension and rarely push. *J Cell Sci*, *109 (Pt 12)*, 2823-2831. http://www.ncbi.nlm.nih.gov/pubmed/9013330

Wieczorek, M., Bechstedt, S., Chaaban, S., & Brouhard, G. (2015). Microtubule-associated proteins control the kinetics of microtubule nucleation. *Nat Cell Biol*, *17*(7), 907-916. https://doi.org/10.1038/ncb3188

Wordeman, L., Wagenbach, M., & von Dassow, G. (2007). MCAK facilitates chromosome movement by promoting kinetochore microtubule turnover. *J Cell Biol*, *179*(5), 869-879. https://doi.org/10.1083/jcb.200707120

Yamashita, N., Morita, M., Legant, W. R., Chen, B., Betzig, E., Yokota, H., & Mimori-Kiyousue, Y. (2015). Three-dimensional tracking of plus-tips by lattice light-sheet microscopy permits the quantification of microtubule growth trajectories within the mitotic apparatus. *J Biomedical Optics*, *20*(10), 101206-101206. https://doi.org/10.1117/1.jbo.20.10.101206

Zar, J. H. (1999). *Biostatistical analysis* (4th ed.). Prentice Hall.

Zelinski, B., & Kierfeld, J. (2013). Cooperative dynamics of microtubule ensembles: Polymerization forces and rescue-induced oscillations. *Phys Rev*, *87*(1). https://doi.org/10.1103/physreve.87.012703